





Quantum correlations in a gravitational collapse simulation with SpheriCo.jl

Benjamin Berczi , **Magdalena Eriksson** ^a, **Thanasis Giannakopoulos** ^{b,c}, **Paul M. Saffin** ^{b,c}

^a*AEC, Institute for Theoretical Physics, University of Bern, Sidlerstrasse 5, CH-3012 Bern, Switzerland*

^b*School of Physics and Astronomy, University of Nottingham, University Park, Nottingham NG7 2RD, United Kingdom*

^c*Nottingham Centre of Gravity, University of Nottingham, University Park, Nottingham, NG7 2RD, United Kingdom*

E-mail: benji.berczi@gmail.com, magdalena.eriksson@unibe.ch,
pmzag1@exmail.nottingham.ac.uk, paul.saffin@nottingham.ac.uk

ABSTRACT: We report on work using a newly developed code, SpheriCo.jl, that computes the gravitational collapse of a spherical scalar field, where the scalar can be either a classical field, or a quantum field operator. By utilising summation-by-parts methods for the numerical derivatives we are able to simulate the collapse longer than was possible previously due to enhanced numerical stability. We present a suite of tests for the code that tests its accuracy and stability, both for the classical and quantum fields. We are able to observe critical behavior of gravitational collapse for the classical setup, in agreement with expected results. The code is also used to compute two-point correlation functions, with results that hint at a non-trivial correlation across the horizon of Hawking quanta.

Contents

1	Introduction	2
2	The classical setup	3
2.1	The classical equations of motion	5
2.2	Classical initial data and boundary conditions	7
3	The semiclassical setup	8
3.1	Quantum equations of motion	9
3.2	Regularized Einstein equations	10
3.3	Quantum initial data and boundary conditions	13
4	Numerical implementation	13
4.1	Finite difference operators	14
4.2	Approximating $\sim 1/r$ terms	15
4.3	Technical details and features	17
5	Code validation: classical setup	19
5.1	Convergence	19
5.2	Robust stability	21
5.3	Constraint violation	23
5.4	Critical phenomena	26
6	Code validation: semiclassical setup	30
6.1	Vacuum without backreaction	30
6.2	Vacuum with backreaction	31
7	Quantum correlators in black hole formation	34
7.1	Without backreaction	36
7.2	With backreaction	38
8	Outlook	38
A	Hyperbolicity of the classical system	44
B	Double null co-ordinates for postprocessing	46
C	Pauli-Villars counterterms	47
D	Additional code testing	49

1 Introduction

The study of the classical problem of gravitational collapse of a scalar field with spherical symmetry has now reached a good level of maturity, with analytic progress [1–4] as well as numerical [5]. In particular, the phenomenon of critical collapse was identified in [6], along with the echos that are observed as the collapse continues [6–8]. Understanding the same system when the classical scalar is promoted to a quantum field is yet to be fully understood, but some progress has been made in this direction [9–12] in two spacetime dimensions. In this semiclassical system we retain a classical geometry, but its dynamics are sourced by the expectation value of the quantum stress-energy tensor. One issue that we face when doing this is the divergence of expectation values of quantities such as the stress-energy tensor, meaning that we need to find suitable regularization techniques that do not spoil the co-ordinate invariance of general relativity. One such approach is a point-splitting procedure [13–16]. Another approach to regularization was taken in [17, 18], where Pauli-Villars ghost fields were introduced, whose contribution to the expectation value of the stress-energy tensor is designed to cancel the divergences. Further study was made in [19] of the effect of radial modes, with reports on the extension to including angular modes presented in [20].

Simulating quantum fields is inherently numerically expensive, as each mode of the quantum field operator must be dynamically evolved and there are as many modes as there are Fourier modes. The restriction to spherical symmetry allows for a large reduction in numerical effort, as the angular part of the calculation may, to some extent, be performed analytically. The cost that one pays is the appearance of spherical co-ordinate singularities, such as $\frac{1}{r}$, in the equations of motion, which must be treated with care in numerical simulations. Here we take the approach of redefining our dynamical variables, along with a summation-by-parts representation of certain operators, following the approach of [21]. With this improvement we then follow [17, 18] in that we use a Pauli-Villars (PV) regularization scheme. We further extend the techniques of [17, 18] by analytically computing the relevant divergent counterterms for the Planck mass and the cosmological constant within this PV regularization scheme.

The numerical approach we use then allows us to simulate the collapsing system for longer times than was possible previously for the semiclassical setup, since we approximate better the equations near the origin. By simulating quantum fields in dynamical backgrounds we may also examine behavior that is not present in the classical system, such as looking for Hawking radiation [22] and correlations in the scalar field between points that are separated across the horizon [23, 24], which are interpreted as correlations between pairs of Hawking quanta. These correlations have also been examined in the case of analogue horizons [25], with correlations in fluctuations developing alongside the appearance of the analogue horizon. In the black hole setting, initial calculations [26] suggest that such correlations may not appear, owing to the singularity swallowing up the Hawking particle that enters the black hole. In this paper we compute such correlations along a spacelike hypersurface in a dynamical, asymptotically flat spacetime, where an apparent horizon forms. For this, we have developed `SpheriCo.jl` [27], an open-access code written in the

Julia programming language [28]. Even though we detect non-trivial correlation between points inside and outside the horizon in certain setups, we believe that a more systematic study is necessary to gain deeper understanding of this behavior and its relation to the various parameters of the problem, such as the size of the apparent horizon.

The structure of the paper is as follows. In section 2 we introduce the equations of motion, together with the initial and boundary data for the classical setup. In section 3 we explain the semiclassical approach of promoting the classical scalar field to a quantum scalar field operator and the subsequent equations of motion we evolve and we describe the regularization scheme, as well as the initial and boundary data. Section 4 is devoted to the numerical implementation followed in `SpheriCo.jl` to solve the classical and semiclassical setups. For the semiclassical case, the implementation includes both scenarios with and without backreaction on the background geometry. In section 5 we present various convergence and physical tests to validate the performance of our code on the classical setup and similarly for the semiclassical one in section 6. Our main new result, the quantum correlators, are in section 7. Finally, we conclude in section 8. Throughout the text, we use the notation $\dot{f} := \partial_t f(t, r)$ and $f' := \partial_r f(t, r)$, but we also use explicit partial derivative notation when it enhances readability. In our simulations we use units where $c = \hbar = 1$. We typically take G_N to be 1 or $1/8\pi$, and we explicitly state our choice in each case.

2 The classical setup

For both the classical and semi-classical simulations we consider a spherically symmetric four-dimensional spacetime, with line element

$$ds^2 = -\alpha^2(t, r)dt^2 + A(t, r)dr^2 + r^2 B(t, r) [d\theta^2 + \sin^2 \theta d\varphi^2], \quad (2.1)$$

where $\alpha(t, r)$ is the lapse function and $A(t, r)$ and $B(t, r)$ are scalar functions. In the classical case, the Einstein field equations are given by

$$G_{ab} + \Lambda g_{ab} = \frac{1}{M_{\text{Pl}}^2} T_{ab}, \quad (2.2)$$

where $G_{ab} := R_{ab} - \frac{1}{2} R g_{ab}$ is the Einstein tensor, T_{ab} is the stress-energy tensor, Λ the cosmological constant, $M_{\text{Pl}} = (8\pi G_N)^{-1/2}$ is the reduced Planck mass and $a, b, \dots = 0, \dots, 3$ run over spacetime dimensions.

Numerical evaluations of the Einstein equations in spherically symmetrical spacetimes are often plagued by co-ordinate singularities at the origin, i.e. $1/r$ terms appearing in the evolution equations. One way to circumvent this issue is by introducing convenient new variables in order to rewrite the (second-order) Einstein equations as first-order differential equations. Rather than evolving the system in terms of the variables α , A and B , we follow [29] and recast it in terms of the variables

$$\begin{aligned} K_A &:= -\frac{1}{2\alpha} \frac{\dot{A}}{A}, & D_A &:= \frac{A'}{A}, & D_\alpha &:= \frac{\alpha'}{\alpha}, \\ K_B &:= -\frac{1}{2\alpha} \frac{\dot{B}}{B}, & D_B &:= \frac{B'}{B}, & \lambda &:= \frac{1}{r} \left(1 - \frac{A}{B} \right), \end{aligned} \quad (2.3)$$

where $\dot{A} := \partial_t A$ and $A' := \partial_r A$. In these co-ordinates, local flatness of the metric at $r = 0$ corresponds to $A(t, 0) = B(t, 0)$, for which $\lambda = 0$, where λ is an auxiliary variable introduced to deal with the co-ordinate singularity at $r = 0$. In addition, the variables K_A and D_A are replaced with K and \tilde{U} respectively, where

$$K := K_A + 2K_B, \quad \tilde{U} := D_A - 2D_B - \frac{4B\lambda}{A}. \quad (2.4)$$

In terms of these variables, the non-vanishing components of the Einstein tensor are

$$G^t_t = \frac{1}{A} \left[D'_B + \frac{1}{r} \left(\lambda + D_B + \tilde{U} - \frac{4\lambda B}{A} \right) - D_B \left(\frac{D_B}{4} + \frac{\tilde{U}}{2} + \frac{2\lambda B}{A} \right) \right] - K_B(2K - 3K_B), \quad (2.5a)$$

$$G^t_r = \frac{2}{\alpha} \left[-K'_B + \left(\frac{1}{r} + \frac{D_B}{2} \right) (K - 3K_B) \right], \quad (2.5b)$$

$$G^r_r = \frac{2}{\alpha} \left[\dot{K}_B - \frac{3\alpha K_B^2}{2} + \frac{\alpha}{2r^2 A} \left(1 - \frac{A}{B} \right) + \frac{\alpha D_B}{2rA} + \frac{\alpha D_B^2}{8A} + \frac{\alpha D_\alpha}{rA} + \frac{\alpha D_B D_\alpha}{2A} \right], \quad (2.5c)$$

$$G^\theta_\theta = \frac{1}{\alpha} (\dot{K} - \dot{K}_B) - K^2 + 3K_B(K - K_B) + \frac{1}{2A} (D'_B + 2D'_\alpha) - \frac{1}{4A} \left[(D_B + 2D_\alpha) \left(\tilde{U} + D_B + \frac{4B\lambda}{A} \right) - 4D_\alpha^2 \right] + \frac{1}{2rA} \left(2D_\alpha - \tilde{U} - \frac{4B\lambda}{A} \right). \quad (2.5d)$$

Here we note that the G^t_t and G^t_r components contain no time derivatives of the evolving variables and are therefore constraint equations. They are referred to as the Hamiltonian and momentum constraint equations, respectively and can be expressed as

$$H := D'_B + \frac{1}{r} \left(\lambda + D_B - \tilde{U} - \frac{4\lambda B}{A} \right) - D_B \left(\frac{D_B}{4} + \frac{\tilde{U}}{2} + \frac{2\lambda B}{A} \right) - AK_B(2K - 3K_B) - AG^t_t = 0, \quad (2.6)$$

$$P := K'_B - \left(\frac{1}{r} + \frac{D_B}{2} \right) (K - K_B) + \frac{\alpha}{2} G^t_r = 0, \quad (2.7)$$

where the terms G^t_t and G^t_r should be understood to be replaced by the components of the stress-energy tensor and cosmological constant term via (2.2).

During a numerical evolution, the constraint equations (2.6) and (2.7) are violated to some degree, which drives the numerical solution away from the physical one and can potentially lead to code instabilities. Having a scheme that forces these constraints to be damped during the evolution can be of great benefit. A famous example is the first successful simulation of black hole binaries [30], where the constraint damping scheme of [31] was utilized. Here, we attempt to minimize the numerical violation of (2.6) and (2.7) by combining the constraint damping scheme of [32] with the regular system of [29]. The former is based on the Z_4 formulation of [33, 34] in which a 4-vector \mathbf{Z} , is added to the

Einstein equations:

$$G_{ab} + \Lambda g_{ab} + \nabla_a Z_b + \nabla_b Z_a = \frac{1}{M_{\text{Pl}}^2} T_{ab} + \kappa_1 [n_a Z_b + n_b Z_a - (1 + \kappa_2) g_{ab} n_c Z^c], \quad (2.8)$$

where κ_1 and κ_2 are parameters that control the constraint damping. The components Z^a are associated with the Hamiltonian and momentum constraints after a 3+1 decomposition of (2.8). n^a are the components of the time-like normal-vector, \mathbf{n} , orthogonal to the spatial hypersurface γ_{ij} in a 3 + 1 (ADM) decomposition of the metric,

$$ds^2 = -\alpha^2 dt^2 + \gamma_{ij} dx^i dx^j, \quad (2.9)$$

where the hypersurface is defined as $\gamma_{ab} := g_{ab} + n_a n_b$ with n_a satisfying $n^a \gamma_{ai} = 0$ and $n^a n_a = -1$.

As a final step to define the classical system, we must fix the redundant gauge dependence of the metric (2.1). The gauge dependence is due to the freedom to choose α , which determines how spacetime is sliced into hypersurfaces of constant time. In order to close the system of the Einstein equations, we impose the Bona-Masso slicing condition [35] via the evolution equation

$$\dot{\alpha} = -2\alpha^2 f(\alpha)[K - 2\Theta], \quad (2.10)$$

where we choose $f(\alpha) = 2/\alpha$, often referred to as the “1 + log” condition [36]. Here $K := \gamma^{ij}(-\gamma^a_i \gamma^b_j \nabla_a n_b) = K_A + 2K_B$ is the trace of the extrinsic curvature and $\Theta := -n^a Z_a$ is the time-like projection of Z_a , which is added to (2.10) in order to ensure that the system is strongly hyperbolic [32].

2.1 The classical equations of motion

We consider a massless spherically symmetric scalar field, $\Phi(t, r)$, with equation of motion $\square\Phi = 0$. In order to also recast the matter sector of the Einstein equations into a first-order differential form, we introduce the variables

$$\Pi := \frac{\sqrt{AB}}{\alpha} \dot{\Phi}, \quad \Psi := \Phi'. \quad (2.11)$$

The stress-energy tensor is $T_{ab} = \partial_a \Phi \partial_b \Phi - \frac{1}{2} g_{ab} g^{cd} \partial_c \Phi \partial_d \Phi$, where the components in the 3 + 1 formulation read

$$\rho := n^a n^b T_{ab} = \frac{1}{2A} \left(\frac{\Pi^2}{B^2} + \Psi^2 \right), \quad (2.12a)$$

$$j_A := -n^a T_{ar} = -\frac{\Pi\Psi}{B\sqrt{A}}, \quad (2.12b)$$

$$S_A := \gamma^{rr} T_{rr} = \frac{1}{2A} \left(\frac{\Pi^2}{B^2} + \Psi^2 \right), \quad (2.12c)$$

$$S_B := \gamma^{\theta\theta} T_{\theta\theta} = \frac{1}{2A} \left(\frac{\Pi^2}{B^2} - \Psi^2 \right), \quad (2.12d)$$

and $\rho := \rho_{\text{ADM}}$ is the ADM energy density and we assume that the classical field Φ is spherically symmetric, i.e. $\partial_\theta \Phi = \partial_\varphi \Phi = 0$. In terms of these variables, the equations of motion for the matter quantities read

$$\dot{\Phi} = \frac{\alpha \Pi}{\sqrt{AB}}, \quad (2.13a)$$

$$\dot{\Pi} = \frac{\alpha B}{\sqrt{A}} \left[\Psi' + \frac{2\Psi}{r} + \Psi \left(D_\alpha - \frac{\tilde{U}}{2} - \frac{2B\lambda}{A} \right) \right], \quad (2.13b)$$

$$\dot{\Psi} = \frac{\alpha}{\sqrt{AB}} \left[\Pi' + \Pi \left(D_\alpha - \tilde{U} - 3D_B - \frac{4B\lambda}{A} \right) \right], \quad (2.13c)$$

and for the gravitational quantities,

$$\dot{A} = -2\alpha A (K - 2K_B), \quad (2.14a)$$

$$\dot{B} = -2\alpha B K_B, \quad (2.14b)$$

$$\dot{D}_B = -2\alpha (K'_B + D_\alpha K_B), \quad (2.14c)$$

$$\begin{aligned} \dot{\tilde{U}} = & -2\alpha \left[K' + 2D_B (3K_B - K) \right. \\ & \left. + D_\alpha (K - 4K_B) + \frac{4B(-3K_B + K)\lambda}{A} + \frac{2j_A}{M_p^2} \right], \end{aligned} \quad (2.14d)$$

$$\begin{aligned} \dot{K} = & \frac{\alpha}{A} \left(\frac{2BD_\alpha \lambda}{A} - D'_\alpha - D_\alpha^2 - \frac{2D_\alpha}{r} + \frac{D_\alpha \tilde{U}}{2} - 2Z'_r \right) + 3\kappa_1 (1 + \kappa_2) \alpha \Theta \\ & - \alpha \left(\frac{4Z_r}{rB} + 4K_B K - 6K_B^2 - K^2 \right) + \frac{\alpha}{M_{\text{Pl}}^2} \left(\frac{S_A}{2} + S_B - \Lambda + \frac{\rho}{2} \right), \end{aligned} \quad (2.14e)$$

$$\begin{aligned} \dot{K}_B = & \frac{\alpha}{A} \left(\frac{BD_B \lambda}{A} + \frac{2B\lambda}{rA} - \frac{D_\alpha}{r} - \frac{D'_B}{2} - \frac{D_\alpha D_B}{2} - \frac{D_B}{r} + \frac{D_B \tilde{U}}{4} - \frac{\lambda}{r} + \frac{\tilde{U}}{2r} \right) \\ & + \alpha \left[\frac{2Z_r}{rB} + K_B K + \frac{1}{2M_{\text{Pl}}^2} (S_A - 2\Lambda - \rho) - \kappa_1 (1 + \kappa_2) \Theta \right], \end{aligned} \quad (2.14f)$$

$$\dot{\lambda} = \frac{\alpha}{B} \left(3AD_B K_B - AD_B K + \frac{Aj_A}{M_{\text{Pl}}^2} + 2AK'_B \right), \quad (2.14g)$$

$$\dot{\alpha} = \alpha (4\Theta - 2K), \quad (2.14h)$$

$$\dot{D}_\alpha = 4\Theta' - 2K', \quad (2.14i)$$

$$\dot{\Theta} = \alpha \left[-\frac{H}{A} + \frac{Z'_r}{A} + \frac{2Z_r}{rB} - \kappa_1 (2 + \kappa_2) \Theta \right], \quad (2.14j)$$

$$\dot{Z}_r = -2\alpha P + \alpha (\Theta' - \kappa_1 Z_r), \quad (2.14k)$$

where $Z_r := \gamma^a_r Z_a$ is the space-like (radial) projection of Z_a . In addition, the Hamiltonian and momentum constraints read

$$\begin{aligned} H = & -\frac{2BD_B \lambda}{A} - \frac{4B\lambda}{rA} - 2AK_B K + 3AK_B^2 + \frac{A\rho}{M_{\text{Pl}}^2} \\ & + D'_B - \frac{1}{2} D_B \tilde{U} - \frac{1}{4} D_B^2 + \frac{D_B}{r} + \frac{\lambda}{r} - \frac{\tilde{U}}{r}, \end{aligned} \quad (2.15a)$$

$$P = - \left(\frac{1}{2} D_B + \frac{1}{r} \right) (K - 3K_B) + \frac{j_A}{2M_{\text{Pl}}^2} + K'_B, \quad (2.15b)$$

which are equated to (2.6) and (2.7), respectively. When simulating the classical system, we will set the cosmological constant to vanish, i.e. $\Lambda = 0$. However, it will be kept non-zero for the semi-classical setup with backreaction described in section 3, where it will act as a counterterm to absorb a divergent contribution from the expectation value of the quantised stress-energy tensor. In summary, the variables of the system can be collected in the state vector

$$\mathbf{u} = \left(\Phi, \Pi, \Psi, A, B, D_B, \tilde{U}, K, K_B, \lambda, \alpha, D_\alpha, \Theta, Z_r \right)^T, \quad (2.16)$$

consisting of matter and gravitational quantities, complemented with Θ and Z_r , which control the violation of the Hamiltonian and momentum constraints, respectively. Here, we have dropped the explicit dependence of the variables on the t, r co-ordinates, for convenience.

2.2 Classical initial data and boundary conditions

To solve the evolution equations in (2.13) and (2.14) we must also provide initial data and boundary conditions. We look for a solution in a domain of interest \mathcal{D} by specifying a time and radius interval for our simulation,

$$\mathcal{D} = \{ (t, r) \in \mathbb{R}^2 : 0 \geq t \geq t_{\text{max}}, 0 \geq r \geq r_{\text{max}} \}. \quad (2.17)$$

The elements of the state vector \mathbf{u} are then provided with initial data at $(t = 0, r)$ and boundary conditions at $(t, r = r_{\text{max}})$.

For the matter sector, we provide as initial data for the scalar field $\Phi(0, r)$ a Gaussian profile of amplitude a , centred symmetrically at a radial distance b from the origin $r = 0$, with a width c , i.e.,

$$\Phi(0, r) = a \left[e^{-\frac{(r-b)^2}{c^2}} + e^{-\frac{(r+b)^2}{c^2}} \right]. \quad (2.18)$$

The two Gaussian functions centred at $r = \pm b$ are used to ensure symmetry of $\Phi(0, r)$ around the origin $r = 0$. The remaining scalar variables are initiated as

$$\Psi(0, r) = \Phi'(0, r), \quad \Pi(0, r) = 0. \quad (2.19)$$

The initial data parameters a , b and c for the classical scalar field profile determine whether a black hole forms in our simulations. Specifically, we interpret black hole formation as the dynamic emergence of an apparent horizon. The apparent horizon is located at the outermost radius where the expansion of null rays $\theta_{\text{exp}} = \frac{1}{\sqrt{A}} \left(\frac{2}{r} + \frac{B'}{B} \right) - 2K_B$ vanishes. The choices of a , b and c that lead to black hole formation are referred to as *supercritical data*, while those that do not result in black hole formation are called *subcritical data*.

On the gravitational side, the geometric quantities are initialised as

$$\begin{aligned} \alpha(0, r) &= B(0, r) = 1, \\ D_\alpha(0, r) &= D_B(0, r) = K(0, r) = K_B(0, r) = 0, \end{aligned} \quad (2.20)$$

for which the initial data for K , K_B and Π trivially satisfy the momentum constraint (2.15b). To satisfy the Hamiltonian constraint (2.15a), we start by setting $A(0,0) = 1$. With the choices (2.20), the non-zero variables in (2.15a) simplify to

$$\tilde{U}(0,r) = \frac{1}{A(0,r)} [A'(0,r) - 4\lambda(0,r)], \quad \lambda(0,r) = \frac{1}{r} [1 - A(0,r)], \quad \rho(0,r) = \frac{\Psi^2(0,r)}{2A(0,r)},$$

where we have used the definitions in (2.3). With these initial values, the Hamiltonian constraint takes the form

$$A'(0,r) = A(0,r) \left[\frac{1 - A(0,r)}{r} + \frac{\Psi^2(0,r)}{2M_{\text{Pl}}^2 r} \right]. \quad (2.21)$$

The initial value for $A(0,r)$ is then obtained by integrating (2.21) over the entire radial domain from $r = 0$ to r_{max} . Finally, the variables related to the constraint damping are initialised as

$$\Theta(0,r) = Z_r(0,r) = 0. \quad (2.22)$$

We understand the spatial boundary at $r = r_{\text{max}}$ as a limitation of our numerical setup rather than a physical boundary. Consequently, we choose to prescribe outgoing boundary conditions at this value. This can be achieved by using the hyperbolicity analysis in appendix A and setting the ingoing characteristic variables of the system to zero. By solving for K , K_B and D_B , we obtain

$$\begin{aligned} D_B &= \sqrt{A}\Theta + Z_r, \\ K_B &= \frac{\sqrt{A}\Theta + Z_r}{2\sqrt{A}}, \\ K &= -\frac{1}{\sqrt{2A}(\alpha - 2)} \left[4\sqrt{2A}\Theta + 2D_\alpha\sqrt{a} - 4\sqrt{A\alpha}\Theta + 4Z_r\sqrt{\alpha} - 2\sqrt{2}Z_r\alpha - D_\alpha\alpha^{3/2} \right]. \end{aligned}$$

where the argument (t, r_{max}) of all ingoing quantities is suppressed. For the scalar field, we set radiative (Sommerfeld) boundary conditions [5] by setting

$$\dot{\mathcal{F}}(t, r_{\text{max}}) = - \left[v_{\text{out}} \mathcal{F}'(t, r) + \frac{\mathcal{F}(t, r)}{r} \right]_{r=r_{\text{max}}}, \quad \mathcal{F} = \{\Phi, \Psi, \Pi\},$$

for $t \in [0, t_{\text{max}}]$ and $v_{\text{out}} = \alpha/\sqrt{A}$ is the speed of the relevant outgoing characteristic variable defined in (A.4).

3 The semiclassical setup

In the semiclassical approximation, the matter fields are promoted to quantum operators $\Phi \rightarrow \hat{\Phi}$, while the gravitational degrees of freedom are treated classically, being sourced by the expectation value of the stress tensor. This approximation holds on large spacetime length scales where quantum gravitational effects are negligible compared to those of the

matter sector.¹ In addition, during the gravitational collapse of a scalar field to a black hole, the curvature increase is expected to be below what is necessary to render quantum-gravity effects important [37].

In the semiclassical framework the Einstein field equations take the form

$$G_{ab} = \frac{1}{M_{\text{Pl}}^2} \left[\langle \chi | \hat{T}_{ab} | \chi \rangle - \Lambda g_{ab} \right], \quad (3.1)$$

where $\hat{T}_{ab} := \partial_a \hat{\Phi} \partial_b \hat{\Phi} - \frac{1}{2} g_{ab} g^{cd} \partial_c \hat{\Phi} \partial_d \hat{\Phi}$ and $|\chi\rangle$ is the quantum state. As we work in a spherically symmetric geometry, it is convenient to expand the quantum field in a basis of spherical harmonics $Y_l^m(\theta, \phi)$ as

$$\hat{\Phi}(t, r, \theta, \varphi) = \sum_{l,m} \int dk \left[\hat{a}_{klm} \tilde{u}_{kl}(t, r) Y_l^m(\theta, \varphi) + \hat{a}_{klm}^\dagger \tilde{u}_{kl}^*(t, r) Y_l^{m*}(\theta, \varphi) \right], \quad (3.2)$$

in terms of a set of mode functions $\tilde{u}_{kl}(t, r)$. We choose the quantum state to be a coherent state $|\chi\rangle$ [17, 18], which has the property that the expectation value of the quantum field operator satisfies the classical field equations and so we call it the classical field and denote it ϕ , i.e. $\phi(t, r) := \langle \chi | \hat{\Phi}(t, r) | \chi \rangle$. In this case, $|\chi\rangle$ is an eigenstate of the annihilation operator \hat{a}_{klm} , such that $\hat{a}_{klm} |\chi\rangle = \mathcal{E} |\chi\rangle$, where \mathcal{E} represents the eigenvalue. The annihilation operator is defined to annihilate the vacuum state $|0\rangle$, i.e. $\hat{a}_{klm} |0\rangle = 0$. In a dynamic spacetime, the vacuum state is ambiguous and we choose to define it by the Minkowski mode functions of the asymptotic past. In practice, this amounts to defining the initial quantum data using the Minkowski spacetime solutions, as described in section 3.3.

3.1 Quantum equations of motion

Analogous to the classical setup, we formulate the equations of motion in a first-order form, in terms of the first temporal and spatial derivatives of the field $\hat{\Phi}$. In addition, it proves convenient to work with the rescaled mode functions

$$u_{kl}(t, r) := \frac{\tilde{u}_{kl}(t, r)}{r^l}. \quad (3.3)$$

We define the conjugate momentum and spatial derivative variables as

$$\pi_{kl}(t, r) := \frac{\sqrt{AB}}{\alpha} \dot{u}_{kl}(t, r), \quad \psi_{kl}(t, r) := u'_{kl}(t, r), \quad (3.4)$$

so that the equations of motion take the form

$$\dot{u}_{kl} = \frac{\alpha}{\sqrt{AB}} \pi_{kl}, \quad (3.5a)$$

$$\dot{\psi}_{kl} = \frac{\alpha}{\sqrt{AB}} \left[\left(D_\alpha - \frac{D_A}{2} - D_B \right) \pi_{kl} + \pi'_{kl} \right], \quad (3.5b)$$

¹Specifically, it is valid when the characteristic length scales of the spacetime are much larger than the Planck length, such as when the Ricci scalar satisfies $R \ll 1/l_{\text{Pl}}^2$. For spacetimes describing collapsing objects like stars or black holes, this condition is met when the mass of the object is much larger than the Planck mass M_{Pl} .

$$\begin{aligned} \dot{\pi}_{kl} = & \frac{\alpha B}{\sqrt{A}} \left[\left(D_\alpha + D_B - \frac{D_A}{2} \right) \left(\frac{l}{r} u_{kl} + \psi_{kl} \right) + \frac{2(l+1)}{r} \psi_{kl} + \psi'_{kl} \right] \\ & + \lambda \frac{l(l+1)}{r} \frac{\alpha B}{\sqrt{A}} u_{kl} - \mu^2 \alpha \sqrt{AB} u_{kl}, \end{aligned} \quad (3.5c)$$

where the argument (t, r) has been suppressed and we have included a mass, μ , for the quantum field. We do this because we will soon need to introduce Pauli-Villars ghost fields in order to regularize the stress-energy tensor and these ghost fields will be massive. We also define

$$D_A := \tilde{U} + 2D_B + \frac{4\lambda B}{A}. \quad (3.6)$$

3.2 Regularized Einstein equations

With a quantised matter sector, the scalar field quantities entering the stress-energy tensor in (2.12) get replaced with quantum expectation values. Concretely, this entails the substitutions

$$\begin{aligned} \Phi^2 & \rightarrow \langle \chi | \hat{\Phi}^2 | \chi \rangle, \\ \Pi^2 & \rightarrow \langle \chi | \hat{\Pi}^2 | \chi \rangle := \frac{AB^2}{\alpha^2} \langle \chi | (\partial_t \hat{\Phi})^2 | \chi \rangle, \\ \Pi\Psi & \rightarrow \langle \chi | \hat{\Pi} \hat{\Psi} | \chi \rangle := \frac{\sqrt{AB}}{\alpha} \langle \chi | \partial_t \hat{\Phi} \partial_r \hat{\Phi} | \chi \rangle, \end{aligned} \quad (3.7)$$

and so on.

The expectation values of the stress-energy tensor contain UV divergences that are directly related to the local curvature of spacetime. These divergences can therefore be regularized using purely geometrical quantities, so that the regularized stress-energy tensor can be expressed as

$$\langle \chi | \hat{T}_{ab} | \chi \rangle_{\text{reg}} = \langle \chi | \hat{T}_{ab} | \chi \rangle - \Lambda g_{ab} - \delta M_{\text{Pl}}^2 G_{ab} - \mathcal{O}(g_{ab} R^2, R_{ac} R^c_b, R_{acdf} R^{fdc}_b), \quad (3.8)$$

for some regularization scheme. Since the lattice breaks diffeomorphism invariance, implementing the continuum curvature-invariant counterterms of (3.8) becomes challenging in practice. One way to address this issue is through Pauli-Villars regularization², which introduces fictitious heavy fields to cancel out the UV divergences while conserving covariance. By incorporating Pauli-Villars fields alongside the scalar field $\hat{\Phi}$ in the simulation, the regularization occurs at the integrand level in momentum space, ensuring that all quantities computed on the lattice are already regularized, meaning that it is not the lattice that provides the regularization.

When introducing Pauli-Villars fields with masses $\mathcal{O}(M_{\text{PV}})$, much larger than any physical mass scales or inverse length scales, the Pauli-Villars mass M_{PV} effectively works as a UV cutoff. On dimensional grounds we then expect that the counterterms in (3.8) to depend on the Pauli-Villars mass as

$$\Lambda \sim M_{\text{PV}}^4, \quad \delta M_{\text{Pl}}^2 \sim M_{\text{PV}}^2, \quad (3.9)$$

²Recently, new point-splitting techniques for numerical simulations in this context have been proposed in [13, 14].

while the coefficients of the higher-order curvature invariants in (3.8) should display at most a logarithmic dependence of M_{PV} . In order to ease our computational efforts, we may set the renormalisation condition, for the range of Pauli-Villars masses we consider, to be that the coefficients of these higher-order geometrical terms vanish. Then we need only determine the counterterms necessary to cancel the quartic and quadratic divergences in (3.9).

While a single Pauli-Villars field is sufficient to cancel the original divergences in the stress-energy tensor components caused by the physical field $\hat{\Phi}$, the added Pauli-Villars field introduces new divergences proportional to the Pauli-Villars mass M_{PV} . As described in detail in [18], it turns out that adding five Pauli-Villars ghost fields is sufficient to fully regularize the system. In order to incorporate the Pauli-Villars ghost fields, the matter Lagrangian can be extended to

$$\mathcal{L}_{\text{matter}} = - \sum_{n=0}^5 (-1)^n \left[\frac{1}{2} \partial_\mu \hat{\Phi}_n \partial^\mu \hat{\Phi}_n + \frac{1}{2} \mu_n^2 \hat{\Phi}_n \right], \quad (3.10)$$

where the index choice $n = 0$ corresponds to the physical field $\hat{\Phi}_0 := \hat{\Phi}$, while $n = 1, \dots, 5$ denote the ghost fields. The mode expansion of the extended scalar sector is analogous to the single-field case in (3.2), i.e.,

$$\hat{\Phi}_n(t, r) = \sum_{l,m} \int dk \left[\hat{a}_{klm;n} \tilde{u}_{kl;n}(t, r) Y_l^m(\theta, \varphi) + \hat{a}_{klm;n}^\dagger \tilde{u}_{kl;n}^*(t, r) Y_l^{m*}(\theta, \varphi) \right]. \quad (3.11)$$

The mass of the physical field is $\mu_0 = 0$ and the masses of the Pauli-Villars fields can be set to

$$\mu_1 = \mu_3 = M_{\text{PV}}, \quad \mu_2 = \mu_4 = \sqrt{3} M_{\text{PV}}, \quad \mu_5 = 2 M_{\text{PV}}, \quad (3.12)$$

so as to regulate the theory.

Due to diffeomorphism invariance of the theory and the Pauli-Villars regulator, any stress tensor counterterm must be expressible as metric/curvature tensors, or their covariant derivatives. The coefficients of these terms may be discovered by computing the stress tensor on different backgrounds. For example, putting the quantum field on Minkowski spacetime allows us to compute the coefficient of the g_{ab} counterterm. However, this geometry will not allow us to compute the G_{ab} counterterm, because G_{ab} vanishes for Minkowski. One way to compute the G_{ab} counterterm is to put the quantum field on a cosmological FRW geometry and if we consider a slowly expanding geometry then we may perform a WKB analysis to compute the coefficient. This calculation is performed in Appendix C and we find the general form of the expectation value of the stress-energy tensor to be

$$\langle \chi | \hat{T}_{ab} | \chi \rangle = \text{finite} - \ln \left(\frac{3^9}{12^{16}} \right) \frac{M_{\text{PV}}^4}{8(2\pi)^2} g_{ab} + \ln \left(\frac{2^4}{3^3} \right) \frac{M_{\text{PV}}^2}{12(2\pi)^2} G_{ab} + \mathcal{O}(g_{ab} R^2, \dots). \quad (3.13)$$

This then sets the counterterms in (3.9) to

$$\Lambda = \ln \left(\frac{3^9}{12^{16}} \right) \frac{M_{\text{PV}}^4}{8(2\pi)^2}, \quad \delta M_{\text{Pl}}^2 = - \ln \left(\frac{2^4}{3^3} \right) \frac{M_{\text{PV}}^2}{12(2\pi)^2}. \quad (3.14)$$

With these counterterms, the effective cosmological constant is set to recover Minkowski spacetime when the matter sector corresponds to vacuum (i.e. when $\phi := \langle \hat{\Phi} \rangle = 0$). In addition, the Planck mass counterterm δM_{Pl}^2 allows us to define an effective Planck mass

$$M_{\text{Pl,eff}}^2 := M_{\text{Pl}}^2 - \ln\left(\frac{2^4}{3^3}\right) \frac{M_{\text{PV}}^2}{12(2\pi)^2}, \quad (3.15)$$

which will be used in the simulation when backreaction is considered.

With the extended matter sector of (3.10), the quantum expectation values entering the stress-energy tensor quantities are

$$\langle \chi | \hat{\Phi}^2 | \chi \rangle = \phi^2 + \frac{\hbar c^2}{4\pi} \sum_{n=0}^5 \sum_l \int dk (-1)^n (2l+1) |\tilde{u}_{kl;n}|^2, \quad (3.16a)$$

$$\langle \chi | (\partial_t \hat{\Phi})^2 | \chi \rangle = (\partial_t \phi)^2 + \frac{\hbar c^2}{4\pi} \sum_{n=0}^5 \sum_l \int dk (-1)^n (2l+1) |\partial_t \tilde{u}_{kl;n}|^2, \quad (3.16b)$$

$$\langle \chi | (\partial_r \hat{\Phi})^2 | \chi \rangle = (\partial_r \phi)^2 + \frac{\hbar c^2}{4\pi} \sum_{n=0}^5 \sum_l \int dk (-1)^n (2l+1) |\partial_r \tilde{u}_{kl;n}|^2, \quad (3.16c)$$

$$\langle \chi | \partial_t \hat{\Phi} \partial_r \hat{\Phi} | \chi \rangle = \partial_t \phi \partial_r \phi + \frac{\hbar c^2}{4\pi} \sum_{n=0}^5 \sum_l \int dk (-1)^n (2l+1)^{\frac{1}{2}} [\partial_t \tilde{u}_{kl;n} \partial_r \tilde{u}_{kl;n}^* + \partial_r \tilde{u}_{kl;n} \partial_t \tilde{u}_{kl;n}^*], \quad (3.16d)$$

$$\langle \chi | (\partial_\theta \hat{\Phi})^2 | \chi \rangle = (\partial_\theta \phi)^2 + \frac{\hbar c^2}{4\pi} \sum_{n=0}^5 \sum_l \int dk (-1)^n \frac{1}{2} l(l+1)(2l+1) |\tilde{u}_{kl;n}|^2, \quad (3.16e)$$

where we have defined $\hat{\mathcal{O}} := \sum_{n=0}^5 \hat{\mathcal{O}}_n$ and the display of \hbar emphasizes the quantum contributions. The temporal and spatial derivatives of $\tilde{u}_{kl;n}$ appearing in (3.16) are related to the rescaled variable $u_{kl;n}$ of (3.3) as

$$\partial_t \tilde{u}_{kl;n} = r^l \frac{\alpha}{\sqrt{AB}} \pi_{kl;n}, \quad \partial_r \tilde{u}_{kl;n} = l r^{l-1} u_{kl;n} + r^l \psi_{kl;n}. \quad (3.17)$$

By using the above expectation values in the expressions for the projections ρ, j_A, S_A and S_B of the stress-energy tensor in (2.12), the new components of the semi-classical stress-energy tensor separates into classical and quantum contributions as

$$\rho = \rho_{\text{cl}} + \frac{\hbar c^2}{4\pi} \rho_{\text{qu}}, \quad (3.18a)$$

$$j_A = j_{A,\text{cl}} + \frac{\hbar c^2}{4\pi} j_{A,\text{qu}}, \quad (3.18b)$$

$$S_A = S_{A,\text{cl}} + \frac{\hbar c^2}{4\pi} S_{A,\text{qu}}, \quad (3.18c)$$

$$S_B = S_{B,\text{cl}} + \frac{\hbar c^2}{4\pi} S_{B,\text{qu}}. \quad (3.18d)$$

The classical components are given as in (2.12) and the quantum components are defined as

$$\rho_{\text{qu}} := \sum_{n=0}^5 \sum_l \int dk (-1)^n \left[\frac{2l+1}{2\alpha^2} |\partial_t \tilde{u}_{kl;n}|^2 + \frac{2l+1}{2A} |\partial_r \tilde{u}_{kl;n}|^2 \right]$$

$$+ \frac{l(l+1)(2l+1)}{2B} |r^{l-1} \tilde{u}_{kl;n}|^2 + \frac{\mu_n^2}{2} |\tilde{u}_{kl;n}|^2 \Big], \quad (3.19a)$$

$$j_{A,\text{qu}} := - \sum_{n=0}^5 \sum_l \int dk (-1)^n \frac{2l+1}{2\alpha} [\partial_t \tilde{u}_{kl;n} \partial_r \tilde{u}_{kl;n} + \partial_r \tilde{u}_{kl;n} \partial_t \tilde{u}_{kl;n}], \quad (3.19b)$$

$$S_{A,\text{qu}} := \sum_{n=0}^5 \sum_l \int dk (-1)^n \left[\frac{2l+1}{2\alpha^2} |\partial_t \tilde{u}_{kl;n}|^2 + \frac{2l+1}{2A} |\partial_r \tilde{u}_{kl;n}|^2 - \frac{l(l+1)(2l+1)}{2B} |r^{l-1} \tilde{u}_{kl;n}|^2 - \frac{\mu_n^2}{2} |\tilde{u}_{kl;n}|^2 \right], \quad (3.19c)$$

$$S_{B,\text{qu}} := \sum_{n=0}^5 \sum_l \int dk (-1)^n \left[\frac{2l+1}{2\alpha^2} |\partial_t \tilde{u}_{kl;n}|^2 + \frac{2l+1}{2A} |\partial_r \tilde{u}_{kl;n}|^2 - \frac{\mu_n^2}{2} |\tilde{u}_{kl;n}|^2 \right]. \quad (3.19d)$$

3.3 Quantum initial data and boundary conditions

The quantum evolution equations must be specified with appropriate initial conditions. Minkowski space initial data provides a natural starting point, as it reflects the asymptotically flat spacetime typical of realistic gravitational collapse scenarios. With this choice, the mode solution to the equation of motion $\square \hat{\Phi}_n = \mu_n^2 \hat{\Phi}_n$ is given by

$$u_{kl;n}^{\text{Mink}}(t, r) = \frac{k}{\sqrt{\pi\omega_n}} \frac{j_l(kr)}{r^l} e^{-i\omega_n t}, \quad (3.20)$$

where $\omega_n = \sqrt{k^2 + \mu_n^2}$ and $j_l(kr)$ are the spherical Bessel functions of the first kind. The initial conditions for the scalar and Pauli-Villars fields at $t = 0$ are then given by

$$u_{kl;n}(0, r) = \frac{k}{\sqrt{\pi\omega_n}} \frac{j_l(kr)}{r^l}, \quad (3.21a)$$

$$\psi_{kl;n}(0, r) = \frac{k}{\sqrt{\pi\omega_n}} \left[\frac{\partial_r j_l(kr)}{r^l} - \frac{l j_l(kr)}{r^{l+1}} \right], \quad (3.21b)$$

$$\pi_{kl;n}(0, r) = -i\omega_n \frac{k}{\sqrt{\pi\omega_n}} \frac{j_l(kr)}{r^l}. \quad (3.21c)$$

The boundary conditions for the quantum modes at r_{max} are the same as those for the classical scalar fields, namely, radiative.

4 Numerical implementation

To simulate the system described by (2.13), (2.14) and (3.5), we discretise it on a uniform grid for the radial co-ordinate $r \in [0, r_{\text{max}}]$. In order to take derivatives at $r = 0$ using finite-difference operators to second-order accuracy, as described in section 4.1, we include two ghost points on the radial grid. Given a maximal radial co-ordinate r_{max} and number of radial points N_r , the grid spacing is $h = r_{\text{max}}/(N_r - 3)$, where the two ghost points are located at the left of the origin $r = 0$, such that the radial grid is $\{-2h, -h, 0, h, \dots, (N_r - 3)h\}$.

When simulating fields of a given wavelength $\tilde{\lambda}$, we must require that the radial grid spacing is much smaller than the smallest wavelength, i.e. $h \ll \tilde{\lambda}_{\min} := 2\pi/k_{\max}$, in order for the lattice to resolve it. For the discrete time step dt we require that $(dt)^{-1} \gg \omega_{\max} := \sqrt{k_{\max}^2 + (\mu_5)^2}$, where $\mu_5 = 2M_{\text{PV}}$ is the mass of the heaviest Pauli-Villars ghost field, in order to have enough resolution in time to resolve the fastest oscillations in the simulation. For the Pauli-Villars masses, we need $M_{\text{PV}} \gg 2\pi/\tilde{\lambda}$, so that the ghost fields do not influence the dynamics of the physical field. In practise, to calculate $\tilde{\lambda}$ for the physical field, we consider twice the radial distance between the maximum of $\Phi(0, r)$ and the location where it has dropped to 5% of the maximum.

4.1 Finite difference operators

We denote as $f_i = f(r_i)$ the discrete approximation of a continuous function $f(r)$ at the point $r = r_i$ of our radial grid. At the beginning of every timestep, we populate the ghost points via

$$f(-h) = f(h), \quad f(-2h) = f(2h),$$

for the even variables and with

$$f(-h) = -f(h), \quad f(-2h) = -f(2h),$$

for the odd ones. We use the centred finite difference (FD) operator

$$D_r f_i := \frac{f_{i+1} - f_{i-1}}{2h}, \quad (4.1)$$

to approximate $\partial_r f(r_i)$ with error $\mathcal{O}(h^2)$ for the grid points $\{0, h, \dots, (N_r - 4)h\}$. At the last grid point $r_{\max} = (N_r - 3)h$, we use the backward finite difference operator

$$D_r f_{N_r-3} := \frac{f_{N_r-3} - f_{N_r-4}}{h}, \quad (4.2)$$

that is accurate to first order. We refer to D_r as the *standard* FD operator and use it to replace all the first order radial derivatives that appear on the right-hand-side (RHS) of our evolution equations.

Both in the classical (2.13)–(2.14) and quantum (3.5) evolution systems there are terms $\sim g/r$, with g a regular odd function. Even though these terms are regular, they can lead to code instabilities that develop in the region around $r = 0$. This problem is especially difficult in the quantum system as the mode number l increases. For very large l the differential equation actually becomes stiff, as the l/r terms in (3.5c) dominate over the derivative terms in size near $r = 0$. Stiff systems can be evolved by using appropriate time integrators such as implicit-explicit Runge-Kutta (RK) schemes [38]. Here, we take a different approach to mitigate this problem by using the second-order accurate summation-by-parts (SBP) operators of [21]. We justify this choice in section 4.2. Denoting these second-order SBP operators as $\tilde{D}_r(l)$, they approximate a radial derivative of an odd function $g(r)$ that is regular at $r = 0$ according to

$$\tilde{D}_r(l) g_i = g'(r_i) + \frac{l g(r_i)}{r_i} + \mathcal{O}(h^2),$$

where l is a positive integer. The operation $\tilde{D}_r(l) g_i$ is calculated via

$$\tilde{D}_r(l) g_i := \frac{w_{i+1} g_{i+1} - w_{i-1} g_{i-1}}{w_i 2h},$$

for the grid points $\{h, \dots, (N_r - 4)h\}$, where w_i are yet-to-be determined weight functions. Since g vanishes on the grid point $r_0 = 0$, we can use the l'Hôpital rule, such that $\tilde{D}_r(l) g_0 = (1 + l) g'(r_0)$, or

$$\tilde{D}_r(l) g_0 := (1 + l) \frac{g_1 - g_{-1}}{2h}.$$

Finally, at the last gridpoint $r_{\max} = (N_r - 3)h$ we apply the backward SBP operator

$$\tilde{D}_r(l) g_{N_r-3} := \frac{w_{N_r-3} g_{N_r-3} - w_{N_r-4} g_{N_r-4}}{w_{N_r-3} h},$$

which is first-order accurate. To complete this calculation, we need the weights w_i . To obtain them we first define $w_i := i^l \bar{w}_i$. Then, we set

$$\bar{w}_0 = \frac{l!}{2^l}, \quad \bar{w}_1 = (1 + l) \bar{w}_0,$$

and solve the recursive relation

$$\bar{w}_i = \frac{2(l+1)}{i} \left(1 - \frac{1}{i}\right)^l \bar{w}_{i-1} + \left(1 - \frac{2}{i}\right)^{l+1} \bar{w}_{i-2},$$

for $2 \leq i \leq N_r - 3$. Note that these weights are different for different values of l . The interested reader can find more details on this and higher-order accurate SBP operators in [21].

4.2 Approximating $\sim 1/r$ terms

The SBP operators of [21] were developed for the wave equation on a flat spacetime (of arbitrary dimensions), which after a spherical harmonic decomposition and a first-order reduction provides the system

$$\dot{\psi} = \pi', \quad \dot{\pi} = \psi' + p \frac{\psi}{r}, \quad (4.3)$$

where p is a positive integer that combines the spherical harmonic index and the space dimension.³ This evolution system admits the energy

$$E = \frac{1}{2} \int_0^R dr (\pi^2 + \psi^2) r^p, \quad (4.4)$$

so well-posedness of the associated initial boundary value problem (with appropriate initial and boundary data) can be shown using this energy. The SBP operators of [21] are constructed in a way that they respect a discrete version of this energy. Consequently, these

³In [21], $p = 2l + n$, where $n + 1$ is the dimension of space and l is a spherical harmonic index.

operators guarantee the stability of the numerical simulation without the need of artificial dissipation. In [21] the theoretically expected convergence rate was demonstrated for second- and fourth-order SBP operators, in a discretized version of the energy norm (4.4) as well as pointwisely for the rescaled variables $r^{p/2}\pi$ and $r^{p/2}\psi$.

The main motivation for choosing these specific SBP operators is that the system (4.3) matches our evolved quantum system (3.5b)–(3.5c) for a flat background, with $\mu = 0$ and $p = 2(l + 1)$. However, since we are interested in non-flat spacetimes, we extrapolate the use of these SBP operators. In particular, we combine D_r and $\tilde{D}_r(l)$ to replace all terms $\sim lg(r)/r$ in the RHS of our evolution equations – both classical and quantum – as

$$\tilde{D}_r(l)g_i - D_r g_i = \frac{lg(r_i)}{r_i} + \mathcal{O}(h^2).$$

For the classical system (2.13)–(2.14), we perform the following replacements:

$$\begin{aligned} \tilde{D}_r(1)\Psi_i - D_r\Psi_i &\simeq \frac{\Psi(r_i)}{r_i}, & \tilde{D}_r(1)Z_{r,i} - D_r Z_{r,i} &\simeq \frac{Z_r(r_i)}{r_i}, \\ \tilde{D}_r(1)\lambda_i - D_r\lambda_i &\simeq \frac{\lambda(r_i)}{r_i}, & \tilde{D}_r(1)D_{B,i} - D_r D_{B,i} &\simeq \frac{D_B(r_i)}{r_i}, \\ \tilde{D}_r(1)D_{\alpha,i} - D_r D_{\alpha,i} &\simeq \frac{D_\alpha(r_i)}{r_i}, & \tilde{D}_r(1)\tilde{U}_i - D_r\tilde{U}_i &\simeq \frac{\tilde{U}(r_i)}{r_i}. \end{aligned} \quad (4.5)$$

where \simeq denotes equality up to $\mathcal{O}(h^2)$ errors. We made the choice to use $\tilde{D}_r(1)$ in all the classical equations, even though in some cases $\tilde{D}_r(2)$ would be more appropriate, because empirically it seemed that otherwise the calculation of the Hamiltonian constraint (2.15a) was somewhat noisy (although the noise had a very small amplitude and it did not ruin the stability of the simulation). We suspect that this is related to the fact that the weights w_i have different values for different l . According to [21], using $\tilde{D}_r(1)$ on a centered grid is identical to the Evans method [39], which has been used previously in critical collapse studies [40].

In the evolution system for the quantum modes (3.5), we make the replacements

$$\tilde{D}_r(l+1)\psi_{kl;n,i} - D_r\psi_{kl;n,i} \simeq \frac{(l+1)\psi_{kl;n,i}(r_i)}{r_i}, \quad (4.6)$$

and

$$\begin{aligned} \tilde{D}_r(l)D_{A,i} - D_r D_{A,i} &\simeq \frac{lD_A(r_i)}{r_i}, & \tilde{D}_r(l)D_{\alpha,i} - D_r D_{\alpha,i} &\simeq \frac{lD_\alpha(r_i)}{r_i}, \\ \tilde{D}_r(l)D_{B,i} - D_r D_{B,i} &\simeq \frac{lD_B(r_i)}{r_i}, & \tilde{D}_r(l)\lambda_i - D_r\lambda_i &\simeq \frac{l\lambda(r_i)}{r_i}, \end{aligned} \quad (4.7)$$

where we first calculate $D_A = \tilde{U} + 2D_B + \frac{4B\lambda}{A}$ from the evolved variables. If we had chosen to replace all the above RHSs with $l(\tilde{D}_r(1) - D_r)$ instead, the simulation becomes unstable as l increases. This is expected since the stiff term $\sim l/r$ is the main contribution of the RHS and it is not accurately resolved.

Finally, we need to calculate the Hamiltonian and momentum constraints (2.15a) and (2.15b) since they are needed for the constraint damping evolution equations of Θ and Z_r ,

respectively. The replacements in (4.5) are sufficient to calculate the Hamiltonian constraint, but not the momentum constraint. We do not have any auxiliary variable similar to λ to regularize the term $(K - 3K_B)/r$ in the momentum constraint (2.15b). Nevertheless, in principle $K - 3K_B$ should vanish at $r = 0$ due to the fact that the space should remain locally flat there (see e.g. chapter 10 of [5]). Even though $K - 3K_B$ is an even function of r , we still use $(\tilde{D}_r(1) - D_r)(K - 3K_B)_i$ to approximate $(K(r_i) - 3K_B(r_i))/r_i$. We have also tried to simply replace its value at $r = 0$ using the l'Hôpital rule, but this approach caused instabilities to develop.

4.3 Technical details and features

Here we outline various details of the structure of `SpheriCo.jl` relevant to the simulations.

Time integration. The time evolution is performed using the method of lines [5] with the third-order Adams-Bashford (AB3) integrator. Since this method requires data from three distinct timesteps, we use the explicit fourth-order Runge-Kutta (RK4) integrator for the first and second timesteps. While AB3 is faster than RK4, it is less accurate and typically requires a smaller timestep to be stable [41]. Nevertheless, given that we need to evolve a large system with as many quantum modes as possible, we chose AB3 for speed.

Artificial dissipation. It is common for finite difference numerical schemes to include artificial dissipation to control high frequency perturbations that are not resolved by the grid spacing. Even though we use SBP operators that in principle do not require artificial dissipation, we still add this option since we heavily extrapolate their use past their original purpose. We use the standard fourth-order Kreiss-Oliger dissipation [42] by modifying the RHS of our evolution equations via

$$\text{RHS}(\partial_t f_i) \rightarrow \text{RHS}(\partial_t f_i) - \sigma \frac{f_{i-2} - 4f_{i-1} + 6f_i - 4f_{i+1} + f_{i+2}}{16h}, \quad (4.8)$$

with $0 < \sigma < 1$, for the grid points $\{0, h, \dots, (N_r - 5)h\}$. Here, it becomes apparent why we include two and not just one ghost point on the left of $r = 0$. For the last two grid points $\{(N_r - 4)h, (N_r - 3)h\}$ we apply

$$\text{RHS}(\partial_t f_i) \rightarrow \text{RHS}(\partial_t f_i) - \sigma \frac{f_{i-4} - 4f_{i-3} + 6f_{i-2} - 4f_{i-1} + f_i}{16h}. \quad (4.9)$$

Initial data generation. When we generate initial data we need to integrate equation (2.21) to obtain $A(r_i)$, after providing $A(r_0)$. The RHS of this equation involves Ψ_i (the discretized version of $\Psi(0, r)$), which is provided only on the grid points. We want to integrate using RK4, such that we provide initial data with error smaller than $\mathcal{O}(h^2)$, which is the dominant error introduced during the evolution by the finite difference operators. Since RK4 involves steps between the grid points r_i and r_{i+1} , we need the value of $\Psi(0, r)$ in this interval. We obtain this using a third-order spline interpolation, provided by the `Julia` package `Interpolations.jl` [43]. Due to the third-order accuracy of the interpolation method, we expect the error in the integrated initial data to be $\mathcal{O}(h^3)$.

Discretized quantum modes and asymptotic flatness. In the discretized version of the quantum field operator $\hat{\Phi}_n$ of (3.11), the integral over momentum k is replaced with a discrete and finite sum, ranging from 0 to k_{\max} . Likewise, the quantum number l ranges from 0 to l_{\max} , with the representation of the quantum field operator becoming more accurate as k_{\max} and l_{\max} increase. The quantum numbers k_{\max} and l_{\max} play different roles in achieving a higher degree of accuracy. As discussed already in [18], it is found empirically that, broadly speaking, l_{\max} parametrizes the spatial region over which the expectation value $\langle \chi | \hat{T}_{ab} | \chi \rangle$ is well-represented, while k_{\max} determines how well $\langle \chi | \hat{T}_{ab} | \chi \rangle$ is represented within that spatial region. In order to find an appropriate choice for l_{\max} and k_{\max} , we note that the vacuum field configuration should correspond to a Minkowski spacetime. By using Minkowski mode functions and setting the classical part to zero ($\phi = 0$), we found empirically that the ratio $l_{\max}/k_{\max} \simeq 3$ leads to a sufficiently large r -domain in which $\langle \chi | \hat{T}_{ab} | \chi \rangle$ vanishes to sufficient accuracy. In order to further guarantee asymptotic flatness in our simulations, we introduce a filter function $F(r)$ that suppress field sources at large r . It is configured as a smooth step function with a transition around a chosen radial point r_{cut} . We define the outermost point of the radial numerical domain that is causally disconnected from r_{\max} as $r_{\text{causal}} := r_{\max} - t_{\max} - dt$. We typically choose $r_{\text{causal}} < r_{\text{cut}} < r_{\max}$. The filter function is set as

$$F(r) = \frac{1}{2} [1 + \tanh(r_{\text{cut}}^p - r^p)], \quad p \in \mathbb{R}, \quad (4.10)$$

which transitions from one to zero around $r = r_{\text{cut}}$, approaching one as $r < r_{\text{cut}}$ and zero as $r > r_{\text{cut}}$, with the steepness controlled by the parameter p . We set $p = 1$, unless stated otherwise explicitly. The filter function is then applied by convolution to the stress-energy tensor quantities in (3.19) as well as the cosmological constant Λ , such that e.g. $\rho_{\text{qu}}(t, r) \rightarrow F(r)\rho_{\text{qu}}(t, r)$ and so on. Empirically we find that our simulations are more robust when the filter is also applied first in the individual quantities of (3.19) by setting $r \rightarrow F(r)r$. This filter is different from artificial dissipation and is used to protect the simulations from numerical instabilities developing at r_{\max} .

Infalling outer boundary. The code provides the option for an evolution setup where the outer boundary r_{\max} is infalling at the speed of light. With this option, the resolution near the origin of the radial domain increases with time, a technique that has been very useful in the study of critical phenomena [7, 44]. In [7] the setup uses a double null foliation, whereas in [44] it is a spacelike formulation which includes a dynamical shift condition, that allows for the outer boundary to drop without regridding. In our formulation, the shift vanishes, so we perform the drop of r_{\max} by a regridding after every timestep by setting $r_{\max} \rightarrow r_{\max} - t$, with t the simulation time and generating a new uniform grid with the same number of points N_r , but smaller h . After each regridding, we need to project all our evolved variables on the new grid, a process that requires interpolation. Again, we use the third-order spline interpolation from `Interpolations.jl`. This numerical algorithm is computationally expensive and it is probably more efficient to include a dynamical shift in the formulation, but we leave this for future development.

Parallelization. Since the evolution equations for the quantum modes (3.5) are independent for each mode $u_{kl;n}$, we can easily parallelize them using Julia’s `Threads.@threads` command. We also parallelize the calculation of the stress-energy tensor expectation values (3.19) in the same way, where we approximate $\int dk$ with $\sum_k dk$. The current version of the code can only run on a CPU. Given how much the independent evolution equations grow with increasing the k_{\max} and l_{\max} of the quantum modes, it seems that adapting the code to also run in parallel on a GPU would be beneficial in terms of speed. This however might include major changes in the architecture of the code, so we leave such an exploration for the future.

Constraint damping. The code provides the choice for damping or no damping of the Hamiltonian and momentum constraints via the variables Θ and Z_r . In principle, the classical evolution system (2.13)–(2.14) damps the Hamiltonian and momentum constraints during the evolution, where the amount of damping is controlled by the parameters κ_1 and κ_2 . However, in our numerical tests we noticed instabilities related to the coupling of Θ and Z_r to (2.14e), (2.14f), (2.14h) and (2.14i) for subcritical data. These instabilities seem to originate from $r = 0$ and so we believe they are related to the way we approximate numerically the Hamiltonian and momentum constraints (2.15a) and (2.15b). In addition, as we show in subsection 5.3, even for supercritical data including constraint damping does not improve the violation of (2.15a) and (2.15b), which defeats their purpose of evolving Θ and Z_r . However, we should mention here that our formulation and evolved variables are different than those in [32], where a conformal splitting is also used (conformal factor in front of the spatial metric). Furthermore, we do not include any damping of reduction constraints, which might also make an important difference [45]. To provide the choice of turning off the damping, we perform $\Theta \rightarrow \text{damping} \times \Theta$ and $Z_r \rightarrow \text{damping} \times Z_r$ (and their derivatives) in the evolution equations (2.14e), (2.14f), (2.14h) and (2.14i). If one sets $\text{damping} = 0$, then there is no coupling between Θ and Z_r to the rest of the equations, even though Θ and Z_r are still evolving and provide information about the amount of constraint violation during the evolution.

5 Code validation: classical setup

We perform a number of tests to check the validity of our code. In this section we focus on the classical setup and perform different convergence tests, as well as physical tests that attempt to reproduce results from the literature.

5.1 Convergence

The dominant error of our numerical scheme comes from the second-order accurate FD operators (both standard and SBP). For any function f we expect $f = f_h + \mathcal{O}(h^2)$, with f the exact solution and f_h the numerical approximation. For the convergence tests, we solve the same system of evolution equations with the same given data, with coarse, medium and fine resolutions and inspect the rate at which the numerical error of the solution decreases. The value of the theoretically expected convergence rate Q is dictated by the resolutions

and the order of accuracy q via

$$Q = \frac{h_c^q - h_m^q}{h_m^q - h_f^q}, \quad (5.1)$$

where h_c , h_m and h_f denote the grid spacing for the coarse, medium and fine resolutions, respectively. We define these grid spacings to correspond to $N_r = \{1027, 2051, 4099\}$, such that we half the grid spacing every time we increase the resolution. These choices of resolutions, combined with the second-order accuracy, yield $Q = 4$ for our tests. If the solution exhibits perfect second-order convergence, then we expect to see $f_c - f_m = Q(f_m - f_f)$, which is what we monitor in the simulations. For each resolution we set $dt = h/8$, which satisfies the Courant–Friedrichs–Lewy (CFL) condition [5]. For these tests, our computational domain is defined by $t_{\max} = 15$ and $r_{\max} = 30$. We present the data only in the part of the radial domain that is causally disconnected from r_{\max} . In principle, we could consider the whole radial domain since we have implemented outgoing boundary conditions that should control numerical reflections at r_{\max} . However, the implemented outgoing boundary conditions for the quantum modes do not preserve their standing wave behavior in Minkowski spacetime, which is a validation test we perform in subsection 6.1, but are useful for numerical stability when backreaction is included. Therefore, in the semiclassical case, we are forced to consider only $r \in [0, r_{\text{causal}}]$ when we interpret our results, and for consistency we choose to do the same in the classical setup as well.

The scalar field initial data are given by (2.18) with $b = 5$, $c = 2$ and $a = 0.5$ for supercritical data or $a = 0.05$ for subcritical data. In this test there is no artificial dissipation, i.e. $\sigma = 0$ in (4.8)–(4.9) and we turn off the constraint damping. We calculate the error between the resolutions by

$$f_{cm} := f_c - \perp_c^m f_m, \quad f_{mf} := \perp_c^m f_m - \perp_c^f f_f, \quad (5.2)$$

where \perp_c^m denotes projection of the medium to the coarse resolution, i.e., we consider only the common points and similarly for \perp_c^f . In figure 1 and figure 2 we see good pointwise convergence of the scalar field Φ , lapse α , absolute value of the Hamiltonian $|H|$ and momentum $|P|$ constraints, for supercritical and subcritical data, respectively.

In appendix A we show that the classical evolution system (2.13)–(2.14) is strongly hyperbolic and so its initial value problem is well-posed in the L^2 -norm (A.10). In addition to the pointwise convergence tests, we also perform norm convergence tests in a discretized version of (A.10), given by (5.3). We obtain the errors as defined in (5.2) for each gridfunction of the state vector \mathbf{u} and calculate

$$\|\mathbf{u}_{cm}\|_{h_c}^2 := \sum_{r=0}^{r_{\text{causal}}} \sum_j \mathbf{u}_{cm,j}^2 h_c, \quad (5.3)$$

and similarly for $\|\mathbf{u}_{mf}\|_{h_c}$. Here j labels the different elements in the state vector \mathbf{u} . In figure 3 we demonstrate good second-order convergence in the discretized L^2 -norm (5.3), for our supercritical and subcritical data with $a = \{0.5, 0.05\}$, $b = 5$ and $c = 2$. In appendix D we repeat these tests including artificial dissipation with $\sigma = 0.02$, which also exhibit good second-order convergence.

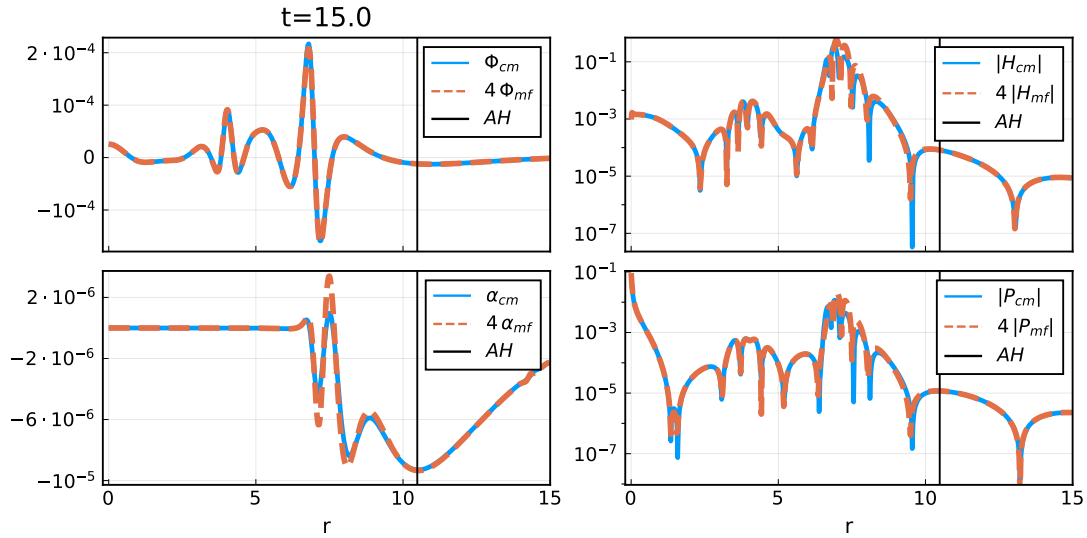


Figure 1. Supercritical data: pointwise convergence for $\Phi, \alpha, |H|, |P|$ at t_{\max} . The overlap of Φ_{cm} with $4\Phi_{mf}$ (similarly for the other gridfunctions) indicates good second-order convergence.

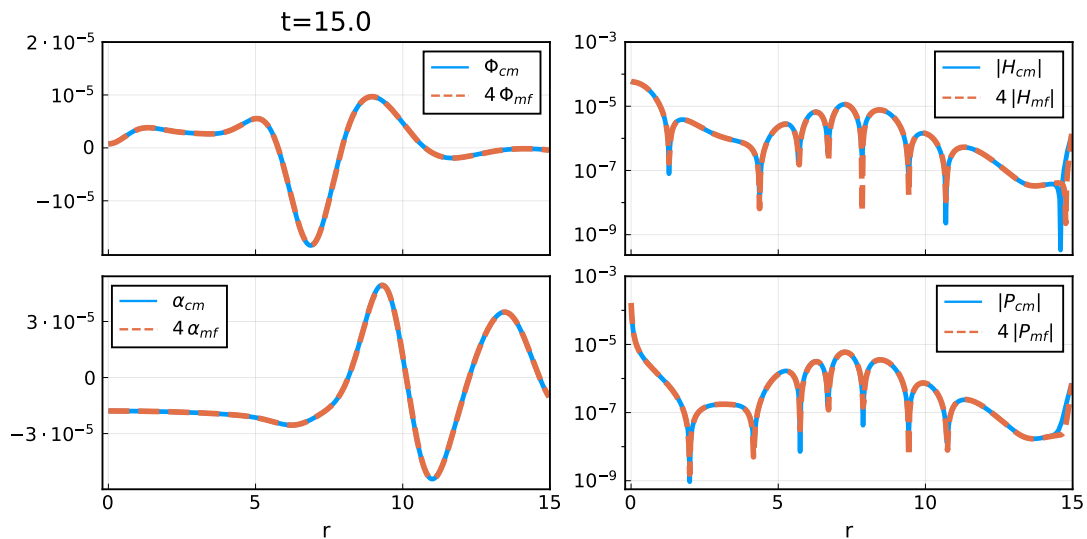


Figure 2. Subcritical data: pointwise convergence for $\Phi, \alpha, |H|, |P|$ at t_{\max} . We see again good second order convergence, indicated by the overlap of the rescaled grid functions.

5.2 Robust stability

We also perform convergence tests with noisy data, typically called *robust stability tests*. These often form standard testbeds for numerical relativity codes [46] and have been widely performed in the literature [47–51]. Briefly, numerical stability can be understood as the discrete analog of well-posedness, where the numerical solution is controlled by the given data, in some discretized norm, in which the initial data are controlled. We will not expand more on numerical stability, but the interested reader can find more information e.g in [52].

For these tests, the initial data are the same as in the previous subsection, with the

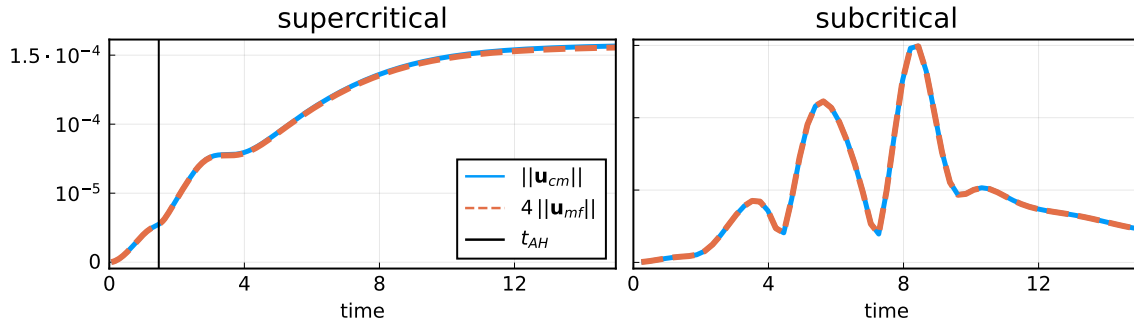


Figure 3. Norm convergence for supercritical (left) and subcritical (right) data, with smooth initial data. Both setups exhibit good second-order convergence, indicated by the good overlap of the rescaled norms.

addition of random noise on top, with amplitude A_h . We add random noise to provide a more demanding test for our code, since often instabilities can develop due to noisy data that are initially small (e.g. due to round-off errors) and increase in time. Hence, the random noise simulates numerical error, in an exaggerated form. To obtain initial data controlled in the L^2 -norm (5.3), we need to scale the amplitude A_h appropriately for the different resolutions. Since we halve the grid spacing every time we increase resolution, we need to drop the amplitude by a factor of four to have initial data that converge to second-order in the L^2 -norm, i.e.,

$$\frac{\|\mathbf{u}_h(0, r_i)\|}{\|\mathbf{u}_{h/2}(0, r_i)\|} = \frac{A_h}{A_{h/2}} = 4. \quad (5.4)$$

Here we have assumed that the smooth part of all the initial data vanishes, for simplicity. While this is not the case in our initial data, it helps to provide an understanding of our chosen scaling for A_h .

For these tests we choose the resolutions $N_r = \{1027, 2051, 4099, 8195, 16387\}$, which we label by $D = \{3, 4, 5, 6, 7\}$ respectively, since we follow $N_r = 128 \cdot 2^D + 3$. We tune the random noise amplitude at resolution D via $A_{h_D} = 10^{-3}/4^D$. With this choice, $A_{h_D}^2$ is above the round-off error $\mathcal{O}(10^{-16})$ for all resolutions apart from $D = 7$, where it is the same order of magnitude as the round-off error. This allows us to test also the non-linear part of the equations, as in [47]. By calculating the discretized L^2 -norm (5.3) and forming ratios like $\|\mathbf{u}_{34}\|/\|\mathbf{u}_{45}\|$ etc., we expect to obtain the convergence rate Q , where here 3, 4, 5 denote the different resolutions. In practice, we consider the test as passed when the numerically computed convergence rate gets closer to the theoretical value of four with increasing resolution and for longer. This is exactly the behavior we see in figure 4 and is qualitatively compatible with the findings of other passed robust stability tests in the literature [48–50]. Furthermore, were an instability triggered in these tests, we would expect to see a rather different picture (the numerical convergence rate would be driven away from the theoretical value faster with increasing resolution, see e.g. the robust stability tests for weakly hyperbolic systems in [51]). The amount of artificial dissipation,

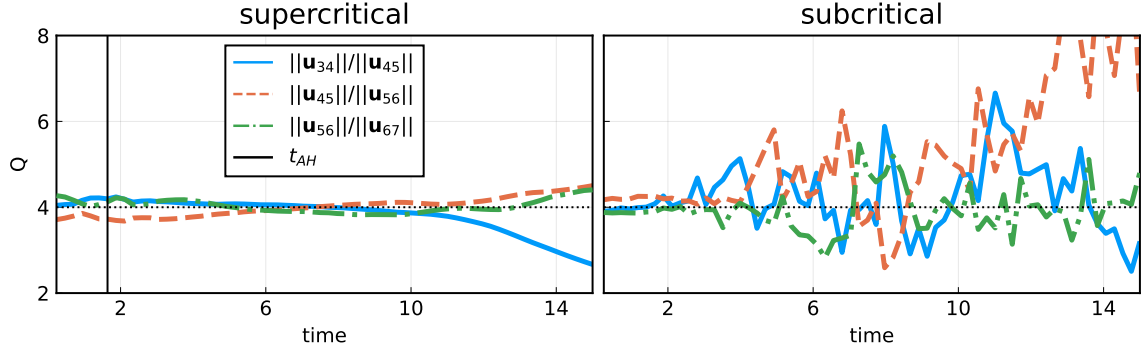


Figure 4. Robust stability tests for supercritical (left) and subcritical (right) data with $b = 5$, $c = 2$ with $a = 0.5$ and $a = 0.05$, respectively, for $\Phi(0, r)$. The amplitude of the random noise is high enough ($A_{h_D} = 10^{-3}/4^D$) to probe both the linear and non-linear terms of the classical setup (2.13)–(2.14). We observe that as the resolution increases, the numerically computed convergence rate approaches the theoretical value of four, and the convergence continues for a longer duration. We interpret this as numerical evidence for stability and convergence of our code. Note that in this setup there is no artificial dissipation.

the CFL, as well as the noise amplitude A_h can affect the picture. In appendix D we provide more robust stability tests.

5.3 Constraint violation

The classical initial data described in section 2.2 exactly satisfy the momentum constraint (2.15b) but introduce some violation of the Hamiltonian constraint (2.15a) due to numerical error. During the evolution, the violations of the Hamiltonian and momentum constraints increase due to accumulation of numerical errors, but as shown in section 5.1, this violation decreases with increasing resolution, following second-order convergence. Here, we wish to test the performance of the constraint damping scheme that we have implemented by including the variables Θ and Z_r with evolution equations (2.14j) and (2.14k), respectively.

Unfortunately, our implementation of the constraint damping is unstable for both supercritical and subcritical data. The instability grows much faster for subcritical data near the origin, whereas for supercritical data the collapse of the lapse function α inside the apparent horizon slows it down and allows us to perform some diagnostic tests. We choose the supercritical initial data of subsection 5.1, namely $a = 0.5$, $b = 5$ and $c = 2$ in (2.18), discretized by $N_r = 4099$, $dt = h/8$, with $r_{\max} = 30$, $t_{\max} = 15$ and no artificial dissipation. To investigate the performance of the implemented constraint damping, we perform a simulation with damping turned off (such that Θ and Z_r do not couple to the rest of the evolution equations) and compare it against simulations with damping turned on, for different values of the parameters κ_1 and κ_2 . We refer to the former as *no-damping* and the latter as *with-damping*. We report with-damping explorations for $(\kappa_1, \kappa_2) = \{(0.002, 0), (0, 0.002), (0.02, 0), (0, 0.02)\}$, which we label by 1 – 4. The no-damping case is labeled with 0.

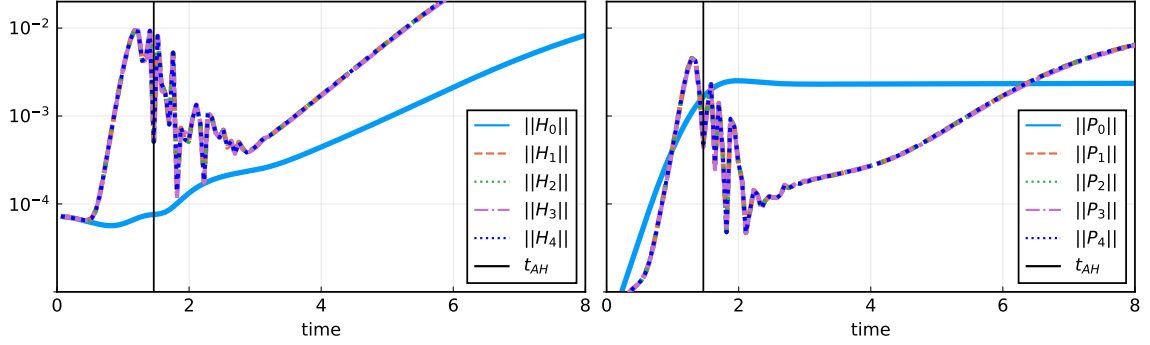


Figure 5. L^2 -norm of the Hamiltonian (left) and momentum (right) constraint violation, in time. We label as 0 the no-damping and as 1 – 4 the with-damping for $(\kappa_1, \kappa_2) = \{(0.002, 0), (0, 0.002), (0.02, 0), (0, 0.02)\}$. The Hamiltonian constraint violation is greater for all the with-damping cases, at all times. The momentum constraint violation is successfully damped for a brief period, for all with-damping simulations.

In all the with-damping simulations the code crashes around $t = 13.9$. In figures 5, 6, 7, 8, we present the results until around $t = 8$, because later the violation grows too big to meaningfully compared with the no-damping case. In figure 5 we show the Hamiltonian- (H) and momentum constraint (P) violation in time, by evaluating the expressions (2.15a), (2.15b), respectively, and compute their discretized L^2 -norm

$$\|f_h\|_h^2 := \sum_{r=0}^{r_{\text{causal}}} f_h^2 h, \quad (5.5)$$

where in this case the grid function is $f_h = \{H, P\}$. In figure 5 see that the Hamiltonian constraint violation is always greater for the with-damping cases, irrespective of the choice of κ_1 and κ_2 . In contrast, the momentum constraint violation, after initially growing larger for the with-damping cases, is successfully damped below that of the no-damping one, up until around $t = 6$. After this, it again grows larger than the no-damping case, which has reached a plateau.

We emphasize that even though the constraint damping we implemented is based on [32], we evolve different variables and we have not implemented damping of the reduction constraints, which could be important [45]. Hence, we also examine the reduction constraint violation in time, by computing their L^2 -norm. For our system, we define the reduction constraints violation as

$$\epsilon(D_A) := \frac{A'}{A} - D_A = \frac{A'}{A} - \tilde{U} - 2D_B - \frac{4B\lambda}{A}, \quad (5.6a)$$

$$\epsilon(D_B) := \frac{B'}{B} - D_B, \quad (5.6b)$$

$$\epsilon(D_\alpha) := \frac{\alpha'}{\alpha} - D_\alpha, \quad (5.6c)$$

which we evaluate in post-processing from our evolved variables, using the standard second-order accurate FD operator (4.1), and (4.2) at r_{max} . In figure 6 we see that the violation of

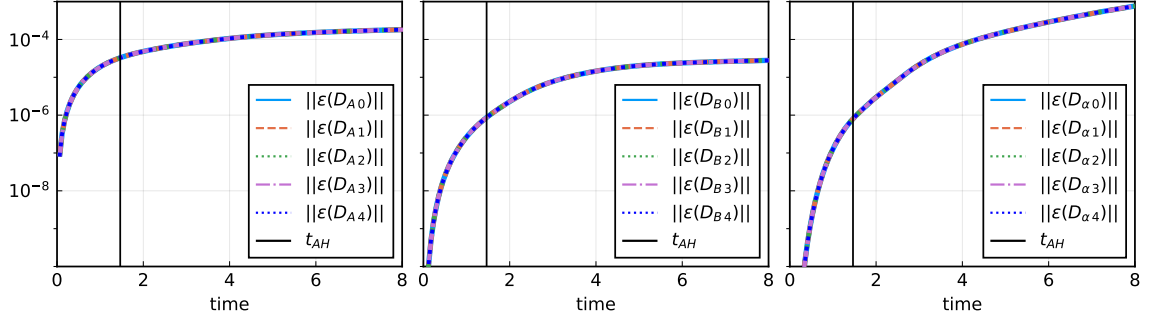


Figure 6. L^2 -norm of the violation for the reduction constraints of D_A (left), D_B (middle) and D_α (right), in time. We label as 0 the no-damping and as 1 – 4 the with-damping for $(\kappa_1, \kappa_2) = \{(0.002, 0), (0, 0.002), (0.02, 0), (0, 0.02)\}$. The violation is similar for all cases, both no- and with-damping.

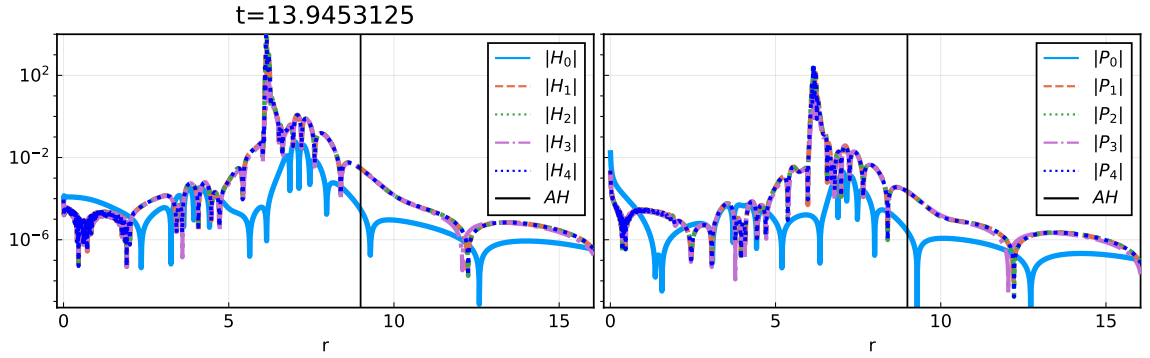


Figure 7. The absolute value of the Hamiltonian (left) and momentum (right) constraint violation, in the radial domain that is causally disconnected from r_{\max} , at $t = 8.02734375$. The subscript 0 labels the no-damping case and the subscripts 1 – 4 the with-damping case for $(\kappa_1, \kappa_2) = \{(0.002, 0), (0, 0.002), (0.02, 0), (0, 0.02)\}$. For both constraints, the violation is greater in the with-damping case, especially in the region $r = (6, 8)$, except from $r = 0$ for the momentum constraint.

the reduction constraints grows during the evolution in the same way for all cases, both no- and with-damping. This is expected, since we have not implemented any scheme for the damping of reduction constraints at this stage. In figures 7 and 8 we show the violation of the Hamiltonian and momentum as well as reduction constraints, respectively, at $t \simeq 8$. For the Hamiltonian and momentum constraints, the violation is greater for the with-damping cases, especially in the region $r = (6, 8)$, which eventually grows significantly, leading to the crashing of the code (the relevant evolved variables Θ and Z_r become very steep in this region). The reduction constraints violation is very similar for all cases, both no- and with-damping, which is expected. We do notice a significant violation in the region $r = (6, 8)$ as well, especially for D_A, D_B . It is possible that this has an important contribution to the growth of the Hamiltonian and momentum constraint violation and eventually the

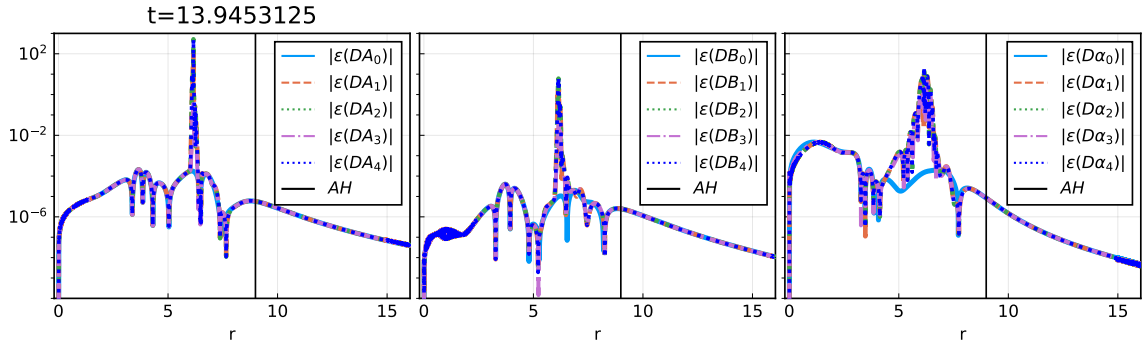


Figure 8. The absolute value of the violation for the reduction constraints of D_A (left), D_B (middle) and D_α (right), in the radial domain that is causally disconnected from r_{\max} , at $t = 8.02734375$. We label as 0 the no-damping and as 1 – 4 the with-damping for $(\kappa_1, \kappa_2) = \{(0.002, 0), (0, 0.002), (0.02, 0), (0, 0.02)\}$. The violation is similar for all cases.

crashing of the code, but it is not clear to us at this stage how much. We have also experimented with the values $(\kappa_1, \kappa_2) = \{(0.002, 0.002), (0.02, 0.02), (0.2, 0), (0, 0.2), (0.2, 0.2)\}$, but their results are very similar. We leave further investigation and development on this topic for future work.

5.4 Critical phenomena

Critical phenomena in gravitational collapse were first discovered numerically by Choptuik [6] and have since then been studied extensively; see [53] for a review and related references. Choptuik’s prototypical example is a massless scalar field, minimally coupled to gravity, the same as our classical setup.

Consider a one-parameter family of initial data, say the classical initial conditions described by (2.18) and (2.19), for fixed position and width and varying amplitude a of the classical scalar field profile. By tuning the amplitude, the evolved data can be supercritical, leading to black hole formation, or subcritical, such that no black hole forms and the spacetime tends to Minkowski spacetime as the energy disperses to infinity. The gravitational critical phenomena occur at the threshold of black hole formation, in between super- and subcritical data and exhibit interesting structure such as echoing (specific oscillations) of the scalar field, power-law scaling of the black hole mass and universality of solutions (that is same behavior of the scalar field irrespective of the family of initial data considered, for near critical solutions).

We explore the performance of `SpheriCo.jl` in the regime of critical phenomena, and focus on the echoing behavior and the universality of solutions. We leave the study of the power-law scaling with our code for future work. To the best of our knowledge, the specific combination of numerical methods we employ – namely, the use of standard FD and SBP operators as described in Section 4 – has not been tested before. Therefore, we aim to assess whether the numerical solution for the classical setup can accurately reproduce well-known physical results. We consider this as a non-trivial test of the code,

and we recognize that the formulation and numerical methods we use are not well-adapted to this problem. Techniques better suited to study criticality may include refinement near the origin via an adaptive mesh as in Choptuik’s original work [6], having an infalling outer boundary (either in characteristic [7] or standard spacelike [44] formulations), using a non-uniform radial grid [54], or using co-ordinates appropriate for self-similar spacetimes [45]. To explore criticality more economically in terms of computational time, we run the simulations with a numerically infalling outer boundary r_{\max} , as described in subsection 4.3, since our metric ansatz (2.1) has a vanishing shift.

The one-parameter family of initial data we choose here is given by (2.18) and (2.19), with $b = 0$, $c = 1$ and a determining whether the initial data is sub- or supercritical. This is the same family used in [54] (in the spherical case), though here a is half the amplitude of the initial Gaussian when it is centered at $r = 0$, due to the definition of our initial data. We refer to this as *initial data family 1*. In appendix D we repeat the analysis for initial data with $b = 5$, $c = 1$ and a tunable, which we refer to as *initial data family 2*. Close to criticality and at $r = 0$, the scalar field is expected to oscillate fast (in terms of the simulation time) around the values ± 0.6 [54], irrespective of the initial data family used (universality of the solution). To have a clearer picture of this oscillation, the similarity time T is often used, defined as

$$T := -\ln(\tau_* - \tau), \quad (5.7)$$

where the proper time τ is given by

$$\tau(t_f, r) = \int_0^{t_f} dt \alpha(t, r), \quad (5.8)$$

where t_f is some final time and τ_* the accumulation time. The latter can be calculated by considering a pair of subsequent zero-crossings τ_n and τ_{n+1} together with another zero-crossing pair τ_m and τ_{m+1} , via

$$\tau_* := \frac{\tau_n \tau_{m+1} - \tau_{n+1} \tau_m}{\tau_n - \tau_{n+1} - \tau_m + \tau_{m+1}}, \quad (5.9)$$

and we refer to e.g. [54] for more details on this.

To have increasing resolution near the origin with time we need to tune t_{\max} and r_{\max} appropriately, such that we have the highest resolution near the accumulation time. Since we do not have prior knowledge of τ_* before the simulation, we make an educated guess based on a few trial simulations. For initial data family 1 we obtain our best results by setting $t_{\max} = 6$ and $r_{\max} = 6.01$ (different values might be even better). We discretize the radial grid with $N_r = 128 \cdot 2^D + 3$ and $D = \{5, 6, 7\}$ and use artificial dissipation with $\sigma = 0.02$. Without artificial dissipation the classification of supercritical and subcritical data is sometimes false near the end of the simulation because of noise near the origin, which possibly arises due to the decreasing grid spacing. We are able to tune the critical amplitude a_* up to five decimals for all three resolutions, that means supercritical and subcritical data are the same in the first five decimal points of a_* . Empirically, it is expected that the critical parameter tuned in numerical explorations depends on the overall accuracy of

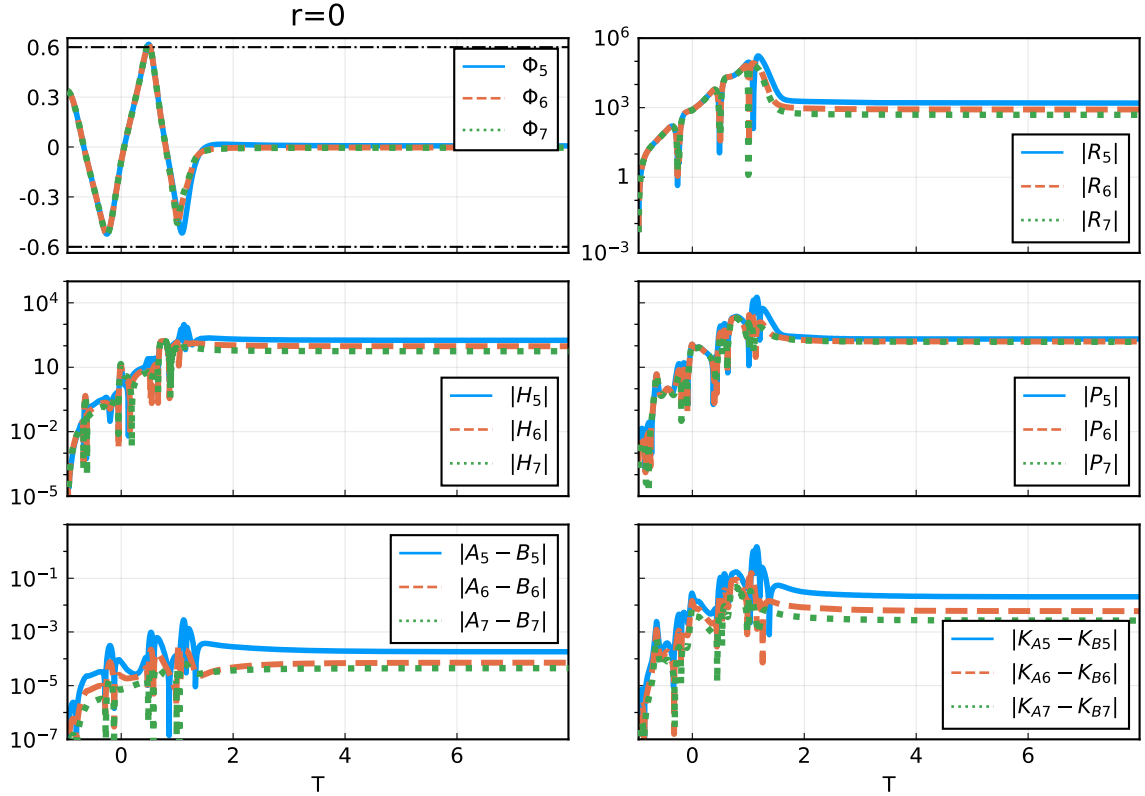


Figure 9. The different quantities monitored against the similarity time T as defined in (5.7), at $r = 0$, for three different resolutions labelled by $D = \{5, 6, 7\}$. Top left: the scalar field, exhibiting a complete oscillation (echo) between ± 0.6 , as expected for near critical solutions. Top right: the absolute value of the Ricci scalar R , the maximum value of which differs at late times between the lowest resolution $D = 5$ and the other two, indicating a possible lack of accuracy. Middle: the absolute value of the Hamiltonian H and momentum P constraints on the left and right, respectively. The violation decreases as we increase the number of points in the radial grid. Bottom: the absolute value of the difference between the metric function A, B (left) and the extrinsic curvature components K_A, K_B (right). The latter is greater than the former by a few orders of magnitude, which could be related to the greater violation of P in comparison to H and the fact that the formulation involves the auxiliary variable λ related to A, B , but nothing similar for K_A, K_B .

the simulation, which in our case translates into a_* being a bit different for different values of D , making convergence tests near criticality hard. The critical amplitude found here is $a_* \in (0.16801640, 0.16801718)$, which differs in the second decimal to that found in [54] (the comparison is between $2a$ in our setup and η of [54]). This difference is not surprising to us, given that our code is not designed for critical collapse explorations.

In figures 9 and 10 we show our analysis for subcritical data with $a = 0.16801640$, for all three resolutions. We focus on the behavior of the different quantities at $r = 0$. Figure 9 shows about one echoing period of the scalar field, oscillating around the values ± 0.6 as expected by the universality of near critical solutions, against the similarity time. The

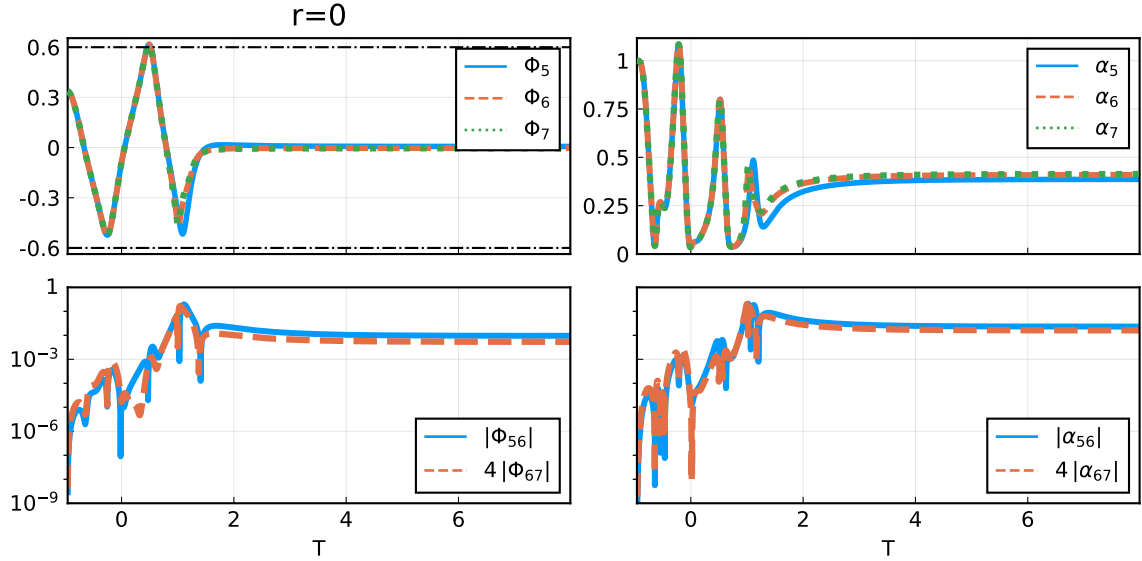


Figure 10. Pointwise convergence at $r = 0$ for the classical scalar field Φ (left) and the lapse function α (right), as a function of the similarity time T . The different resolutions $D = \{5, 6, 7\}$ are denoted with the respective D in the subscript. The numerical error (bottom) is computed by taking the difference between the numerical solutions of two different resolutions, denoted by both their D labels in the subscript. The good overlap of the rescaled errors in the bottom, indicates good second-order convergence. The rescaling factor comes from the theoretically expected convergence rate computed in (5.1).

same oscillating behavior is also apparent in initial data family 2, shown in appendix D. Additionally, figure 9 shows the Ricci scalar R , as well as the Hamiltonian and momentum constraint violations H and P . We also monitor the difference between the metric functions A and B as well as the components of the extrinsic curvature K_A and K_B . We do this to assess if the introduction of the auxiliary variable λ defined in (2.3), which drives $A = B$ at $r = 0$, has an effect on the violation of the Hamiltonian constraint H (2.15a). In contrast, there is no such auxiliary variable for K_A, K_B (the evolved variable here is $K = K_A + 2K_B$) but the term $K_A - K_B$ affects the violation of momentum constraint P , as seen from the definition (2.15b).

Interestingly, in figure 9 we see that the difference between K_A and K_B at $r = 0$ is a few orders of magnitude larger than that of A and B , and similarly for P in comparison to H . This result suggests that introducing another auxiliary variable similar to λ but for K_A and K_B might lead to a smaller momentum constraint violation, allowing for a better simulation of near critical phenomena. In the current version of the code, we see that the maximum momentum constraint violation for the smallest resolution is only an order of magnitude lower than the Ricci scalar at $r = 0$, which is often interpreted as having insufficient accuracy to model critical phenomena [55]. The introduction of an auxiliary variable for K_A, K_B similar to λ has already been suggested and successfully used [56]. In figure 10 we see good second-order convergence for the scalar field and lapse at $r = 0$,

against the similarity time.

6 Code validation: semiclassical setup

We also perform tests to examine the validity of our code in the semiclassical setup. Although our primary interest lies in black hole spacetimes or the regime near criticality, we first focus on Minkowski spacetime, where the behavior of the quantum modes is well-known and well-understood.

6.1 Vacuum without backreaction

We consider the setup where the classical scalar field is vanishing, so that the spacetime is Minkowski. We perform an evolution of the quantum modes in Minkowski spacetime, neglecting backreaction. The classical geometry is obtained for every timestep of the evolution by running `SpheriCo.jl` with $a = 0$ for the classical initial data (2.18). For the quantum modes we choose $k_{\max} = 10$, $l_{\max} = 60$, $dk = \pi/30$ and $M_{\text{PV}} = 1$. The ratio l_{\max}/k_{\max} here is 6 instead of 3, which is our choice in general, just to make less expensive the calculation of norm (6.2). This ratio is not important here as we are not considering backreaction. As mentioned in subsection 3.3, the analytical solution in vacuum for the quantum modes is

$$u_{kl;n}^{\text{Mink}}(t, r) = e^{-i\omega_n t} \frac{k}{\sqrt{\pi\omega_n}} \frac{j_l(kr)}{r^l}, \quad (6.1a)$$

$$\psi_{kl;n}^{\text{Mink}}(t, r) = e^{-i\omega_n t} \frac{k}{\sqrt{\pi\omega_n}} \left[\frac{\partial_r j_l(kr)}{r^l} - \frac{l j_l(kr)}{r^{l+1}} \right], \quad (6.1b)$$

$$\pi_{kl;n}^{\text{Mink}}(t, r) = -i\omega_n e^{-i\omega_n t} \frac{k}{\sqrt{\pi\omega_n}} \frac{j_l(kr)}{r^l}, \quad (6.1c)$$

with $\omega_n = \sqrt{k^2 + \mu_n^2}$. We simulate this setup with $r_{\max} = 30$ fixed, $t_{\max} = 10$, $N_r = 128 \cdot 2^D + 3$, for $D = \{2, 3, 4\}$ and $dt_D = h_D/16$ in all resolutions, without any artificial dissipation. In this test we use the convention $1/M_{\text{Pl}}^2 = 1$ which was also used in [18]. We want to compare the numerical against the analytical solution and examine the rate at which the former converges to the latter, with increasing resolution. For this we calculate the following norm

$$\begin{aligned} \|\mathbf{u}_{\text{qu}}\|_D^2(t) := & \sum_{kl n} \sum_{r=0}^{r_{\text{causal}}} h_D \left[(u_{kl;n,D}(t, r) - u_{kl;n}^{\text{Mink}}(t, r)) (u_{kl;n,D}(t, r) - u_{kl;n}^{\text{Mink}}(t, r))^* \right. \\ & + (\psi_{kl;n,D}(t, r) - \psi_{kl;n}^{\text{Mink}}(t, r)) (\psi_{kl;n,D}(t, r) - \psi_{kl;n}^{\text{Mink}}(t, r))^* \\ & \left. + (\pi_{kl;n,D}(t, r) - \pi_{kl;n}^{\text{Mink}}(t, r)) (\pi_{kl;n,D}(t, r) - \pi_{kl;n}^{\text{Mink}}(t, r))^* \right], \end{aligned} \quad (6.2)$$

where \mathbf{u}_{qu} is the part of the state vector that contains all the quantum field modes, the subscript D denotes the numerical solution at resolution D , the superscript $*$ the complex conjugate and t, r are to be understood as the evolution timestep and radial grid point where the data is saved at each resolution. Similarly to subsection 5.1, the expected

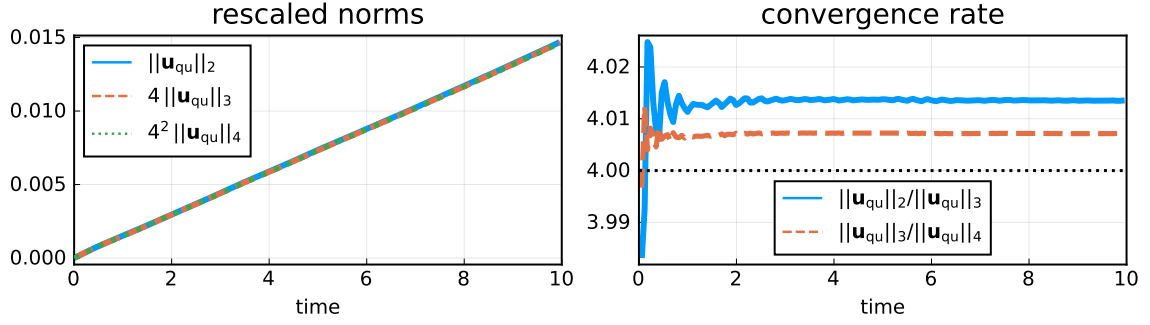


Figure 11. The rescaled norm (6.2) (left) and exact convergence rate (right), for a semiclassical simulation with vanishing classical scalar field, $k_{\max} = 10$, $l_{\max} = 60$ and $M_{\text{PV}} = 1$. The simulation exhibits good second-order convergence for the whole simulation time, when all the quantum modes are included.

convergence rate for this test is

$$Q = \frac{h_D^2}{h_{D+1}^2} = \frac{h_D^2}{h_D^2/4} = 4, \quad (6.3)$$

which we call *exact convergence rate* since the comparison is against an exact (analytic) solution and not a numerical one. Figure 11 illustrates the second-order convergence of the numerical solution for (6.1) in the norm (6.2), including all the evolved modes. However, we know that the modes with high l and μ_5 oscillate faster and so are harder to simulate accurately. Furthermore, we know that the amplitude of the modes with high l is smaller than those with lower and hence a possible lack of convergence for high l might not be seen in the norm (6.2). For this reason we also examine convergence in the norm

$$\begin{aligned} \|\mathbf{u}_{\text{qu}}\|_{D;60,5}^2 &= \sum_k \sum_{r=0}^{r_{\text{causal}}} h_D [(u_{k60;5,D} - u_{k60;5}^{\text{Mink}}) (u_{k60;5,D} - u_{k60;5}^{\text{Mink}})^* \\ &\quad + (\psi_{k60;5,D} - \psi_{k60;5}^{\text{Mink}}) (\psi_{k60;5,D} - \psi_{k60;5}^{\text{Mink}})^* \\ &\quad + (\pi_{k60;5,D} - \pi_{k60;5}^{\text{Mink}}) (\pi_{k60;5,D} - \pi_{k60;5}^{\text{Mink}})^*], \end{aligned} \quad (6.4)$$

which is the part of the state vector that includes all the quantum modes with $l = 60$ and $n = 5$ and we have suppressed the argument (t, r) . Figure 12 shows the convergence of this part of the numerical solution in the norm (6.4). Up until $t \simeq 7.9$ the solution exhibits good second-order convergence, which improves with increasing resolution. However, around $t \simeq 7.9$, there is a fast loss of convergence, which is not captured by the norm (6.2), possibly because the slower modes that continue to converge well dominate the norm, as they have a much greater amplitude.

6.2 Vacuum with backreaction

We also test the evolution of vacuum initial data with backreaction. In this scenario, we wish to test if the numerical solution remains closer to Minkowski with an increasing

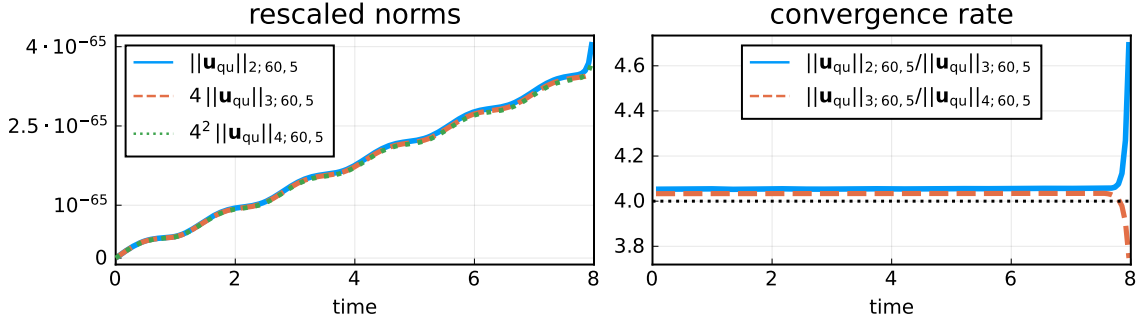


Figure 12. The rescaled norm (6.4) that includes only the fastest oscillating quantum modes (left) and the respective exact convergence rate (right), for a semiclassical simulation with vanishing classical scalar field, $k_{\max} = 10$, $l_{\max} = 60$ and $M_{\text{PV}} = 1$. These modes exhibit good second-order convergence for a shorter part of the simulations, but this effect is not seen in the norm (6.2), due to their small relative amplitude.

number of quantum modes backreacting on the geometry. We set $a = 0$ for the classical scalar initial data (2.18), $r_{\max} = 30$, $t_{\max} = 10$, $dk = \pi/30$, $dt = h/16$, $N_r = 128 \cdot 2^D + 3$ with $D = 3$ and no artificial dissipation. In the filter function (4.10), we set $r_{\text{cut}} = 20$. When we increase the number of quantum modes we use $(k_{\max}, l_{\max}) = \{(5, 15), (10, 30), (20, 60)\}$. This choice keeps the ratio $l_{\max}/k_{\max} = 3$ fixed, which we found empirically allows us to model accurately the backreaction in the region up to $r \simeq \pi/dk$. By this we mean that for a vanishing classical scalar field, the stress-energy tensor components at initial time have a flat profile in this region, as described in [18].

To measure the deviation of the numerical solution to the Minkowski spacetime solution we calculate the following norm

$$\begin{aligned}
\|\mathbf{u}\|_{k_{\max}, l_{\max}}^2(t) := & \sum_{r=0}^{r_f} h \left[(A(t, r) - A^{\text{Mink}}(t, r))^2 + (B(t, r) - B^{\text{Mink}}(t, r))^2 \right. \\
& + (D_B(t, r) - D_B^{\text{Mink}}(t, r))^2 + \left(\tilde{U}(t, r) - \tilde{U}^{\text{Mink}}(t, r) \right)^2 \\
& + (K(t, r) - K^{\text{Mink}}(t, r))^2 + (K_B(t, r) - K_B^{\text{Mink}}(t, r))^2 \\
& + (\lambda(t, r) - \lambda^{\text{Mink}}(t, r))^2 + (\alpha(t, r) - \alpha^{\text{Mink}}(t, r))^2 \\
& \left. + (D_\alpha(t, r) - D_\alpha^{\text{Mink}}(t, r))^2 \right], \tag{6.5}
\end{aligned}$$

where r_f is some final radial grid point. We perform this test for $M_{\text{PV}} = \{0.1, 1, 2\}$ and we choose $r_f = 10$ for the upper limit in (6.5), so that we are safely within the region where backreaction is well-modeled and causally disconnected from the outer boundary r_{\max} and r_{cut} of the filter function (4.10). In figure 13 we show the results of this test. We see that with increasing number of quantum modes backreacting to the classical geometry, the numerical solution is closer to that of Minkowski spacetime during the evolution, i.e., the size of the deviation from Minkowski as measured with the norm (6.5) decreases. We

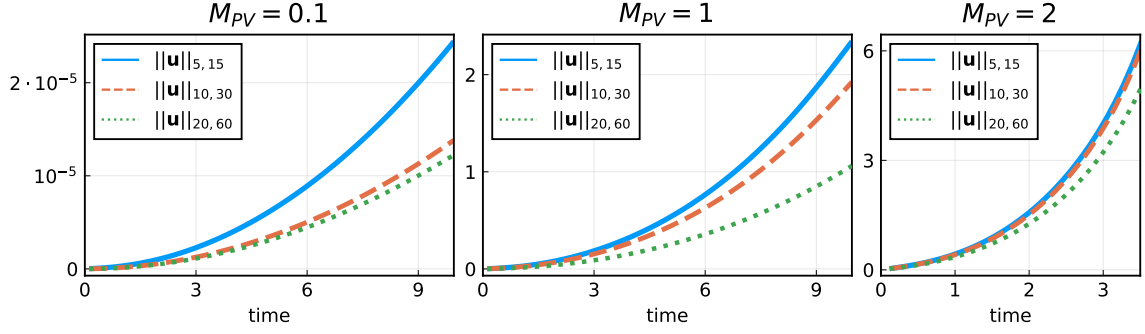


Figure 13. The deviation of the numerical solution with backreaction from Minkowski, as measured by the norm $\|\mathbf{u}\|_{k_{\max}, l_{\max}}$ (6.5). The deviation decreases with increasing number of quantum modes backreacting and with smaller values of M_{PV} .

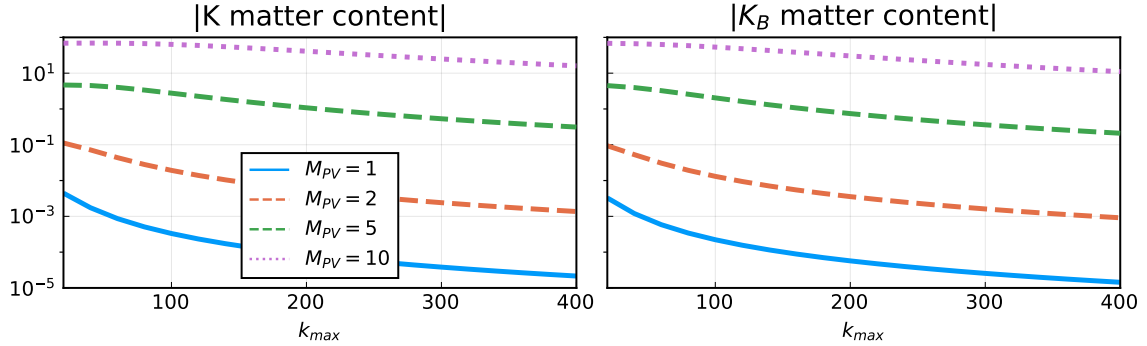


Figure 14. The matter content for the RHS of K (left) and K_B (right) for Minkowski classical initial data at $(t, r) = (0, 0)$ for increasing k_{\max} , with $l_{\max} = 10$ and $M_{\text{PV}} = \{1, 2, 5, 10\}$.

also see that this deviation is significantly smaller for low values of M_{PV} and even detect instabilities that lead to the simulation crashing for $M_{\text{PV}} = 2$.

To better understand the interaction between the values of M_{PV} , k_{\max} and l_{\max} in backreaction, we also inspect the quality of the initial data, for different values of M_{PV} , fixed l_{\max} and increasing k_{\max} . Based on the results of [18], empirically we know that keeping l_{\max} fixed and increasing k_{\max} provides a better approximation of the quantum operator, but for a smaller region of r , close to $r = 0$. If instead k_{\max} is fixed and l_{\max} increases, we get a poorer approximation of the quantum operator but for a larger r region. This result also depends on the value of dk . We want to understand how fast the matter content of the evolution equation (2.14e) for K and (2.14f) for K_B tend to zero at $t = r = 0$, with increasing k_{\max} and fixed l_{\max} . These are given by

$$\frac{1}{M_{\text{Pl}}^2} \left(\frac{S_A}{2} + S_B - \Lambda + \frac{\rho}{2} \right), \quad \frac{1}{2M_{\text{Pl}}^2} (S_A - 2\Lambda - \rho), \quad (6.6)$$

for (2.14e) and (2.14f), respectively. This behavior can inform us which are the possible realistic Pauli-Villars masses that we can use in backreaction. If the deviation of these

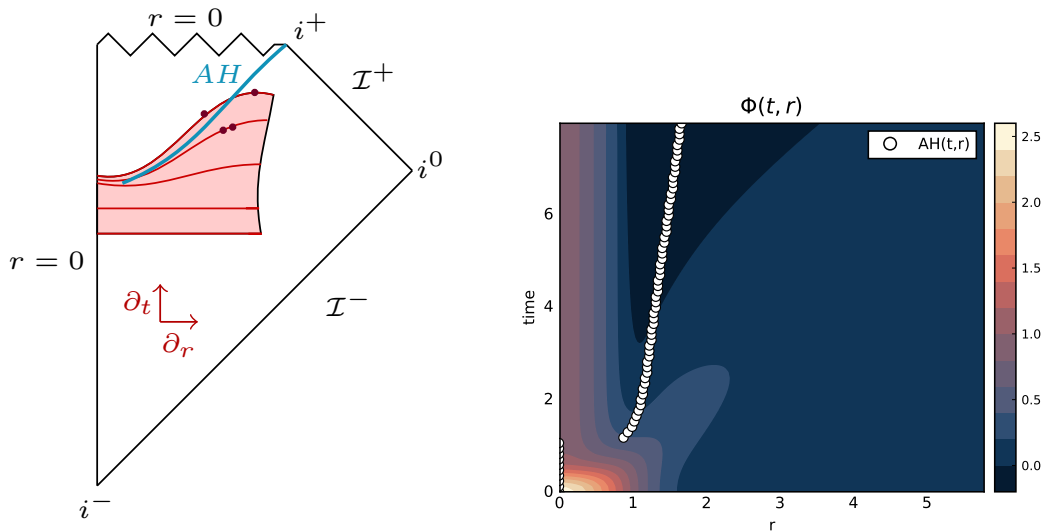


Figure 15. Left: part of the conformal diagram of an asymptotically flat spacetime, where an apparent horizon dynamically forms. The red region depicts our numerical domain and the dots are two arbitrary points on a spacelike hypersurface (solid red lines) for which we calculate the equal time quantum correlators. Right: the evolution of a scalar field in the $t - r$ plane, with $a = 1.25$, $b = 0$ and $c = 1$, which leads to a dynamical formation of an apparent horizon (white circles).

matter contents at the level of initial data and for $r = 0$ is significantly far from zero for a given M_{PV} , then we cannot hope to have a good time evolution that would pass our earlier Minkowski consistency test, let alone trust it in more interesting scenarios. We explore this behavior for $l_{\text{max}} = 10$, $k_{\text{max}} = [20, 400]$, $M_{\text{PV}} = \{1, 2, 5, 10\}$, $dk = \pi/r_{\text{max}}$ and $r_{\text{max}} = 30$. In figure 14 we see that the K and K_B matter contents (6.6) converge slower to zero with increasing values of M_{PV} . Therefore, to study quantum correlators we use $M_{\text{PV}} = 1$, since larger values of M_{PV} provide less accurate approximations of the quantum operator, for realistic values of k_{max} and l_{max} . In our physical explorations of section 7, we set k_{max} at most to 30.

7 Quantum correlators in black hole formation

Hawking radiation is a phenomenon that requires quantum fields in the environment of a black hole. Using `SpheriCo.jl` we can explore such scenarios, where the apparent horizon of a black hole dynamically forms, as for instance seen in the right of figure 15. In this scenario, we can examine if there are any non-trivial correlations of the scalar field operator at different spacetime events across the horizon of the black hole. Such a correlation of the scalar field may be interpreted as correlating pairs of Hawking quanta. Videos from simulations of this section can be found in [57].

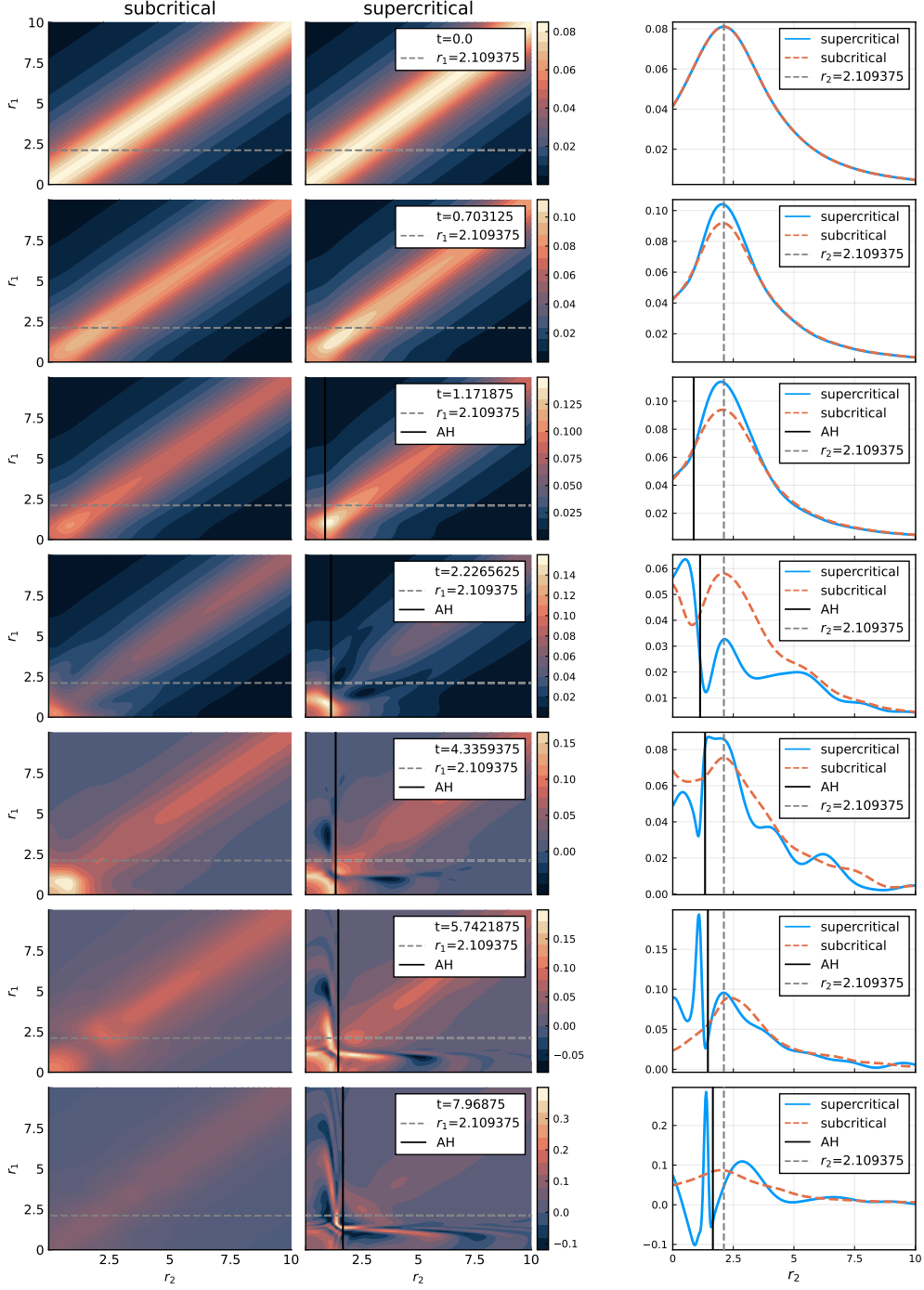


Figure 16. The real part of the equal time correlator (7.1) for $\Phi(0, r)$ with $b = 0$, $c = 1$, $k_{\max} = 30$, $l_{\max} = 90$ and $M_{\text{PV}} = 1$ without backreaction. The subcritical case (left) has $a = 0.75$ and the supercritical (middle) $a = 1.25$. The correlation of point $r_1 = 2.109375$ with the rest of the domain, at different timesteps, for both sub- and supercritical setups, is shown on the right. For $r_1 = r_2$ we see the correlation of the chosen point to itself.

7.1 Without backreaction

From the two-point correlation function (3.16a) of the quantum field, we define the correlation function C of the fluctuations around the field expectation value ϕ , i.e.,

$$\begin{aligned} C(t_1, t_2; r_1, r_2) &:= \langle \chi | \hat{\Phi}(t_1, r_1) \hat{\Phi}(t_2, r_2) | \chi \rangle - \phi(t_1, r_1) \phi(t_2, r_2) \\ &= \frac{\hbar c^2}{4\pi} \int dk \sum_{n=0}^5 \sum_{l=0}^{l_{\max}} (-1)^n (2l+1) [\tilde{u}_{kl;n}(t_1, r_1) \tilde{u}_{kl;n}^*(t_2, r_2)]. \end{aligned} \quad (7.1)$$

In the following we are interested in equal-time correlations, and so we will evaluate $C(t_1, t_2; r_1, r_2) = C(t; r_1, r_2)$ at time $t_1 = t_2 = t$. In `SpheriCo.jl`, one can also calculate analogous correlation functions as (7.1) for $\partial_t \tilde{u}_{kl;n}$, $\partial_r \tilde{u}_{kl;n}$, $\pi_{kl;n}$ and $\psi_{kl;n}$, by replacing $\tilde{u}_{kl;n}$ with the appropriate variable.

We perform simulations for both a sub- and supercritical setup, without backreaction and calculate the correlator (7.1) at different times. For these simulations, the scalar pulse is initially set with $b = 0$, $c = 1$ and $a = 0.75$ for the subcritical and $a = 1.25$ for the supercritical case, respectively. We also set $k_{\max} = 30$, $l_{\max} = 90$, $dk = \pi/r_{\max}$, with $r_{\max} = 30$ and $M_{\text{PV}} = 1$. The radial grid consists of $N_r = 1027$ points, the artificial dissipation is $\sigma = 0.02$ and the timestep is set to $dt = h/16$. In figure 16 we present our findings. We shall call the *main diagonal* the one that connects the bottom left corner to the top right corner in the heatmaps of figure 16. At $t = 0$ the correlation is the same in both cases and it is the same as in Minkowski, which is more prominent on the main diagonal, indicating maximum correlation of a point to itself. For the supercritical case, as time progresses, we see that the correlator exhibits a non-trivial behavior away from the main diagonal, that correlates a point inside the apparent horizon with one outside. We use the terminology of [25] and refer to these as *tongues*. These tongues of correlation grow in size as time progresses, also acquiring negative values. In contrast, in the subcritical case, after an initial increase in size of the correlator around the origin of the heatmap, and a mild oscillatory behavior, the correlator relaxes back to a profile similar to its original one.

Hawking radiation has been studied and observed in analogue black holes [25, 58, 59]. There are both similarities and differences between the correlators we compute in the supercritical case, and those from analogue systems with a horizon. In both cases there is significant non-trivial behavior of the correlator away from the main diagonal, which has an oscillatory profile and takes both positive and negative values. However, in analogue systems the correlator maintains a dominant profile in the main diagonal at all times, which is not the case in our simulations. In addition, the non-trivial correlation away from the main diagonal appears in greater angles in the analogue system compared to ours. In our case we expect the details of the correlation tongues to depend on the choice of lapse function, but the qualitative structure of correlations outside and within the horizon to remain. It is possible that our picture is greatly affected by the collapse of the lapse inside the apparent horizon, which effectively freezes the simulation near the origin of our computational domain, leading to that the tongues appear at smaller angles. However, in analogue systems there is no singularity, which might be responsible for the quantitative

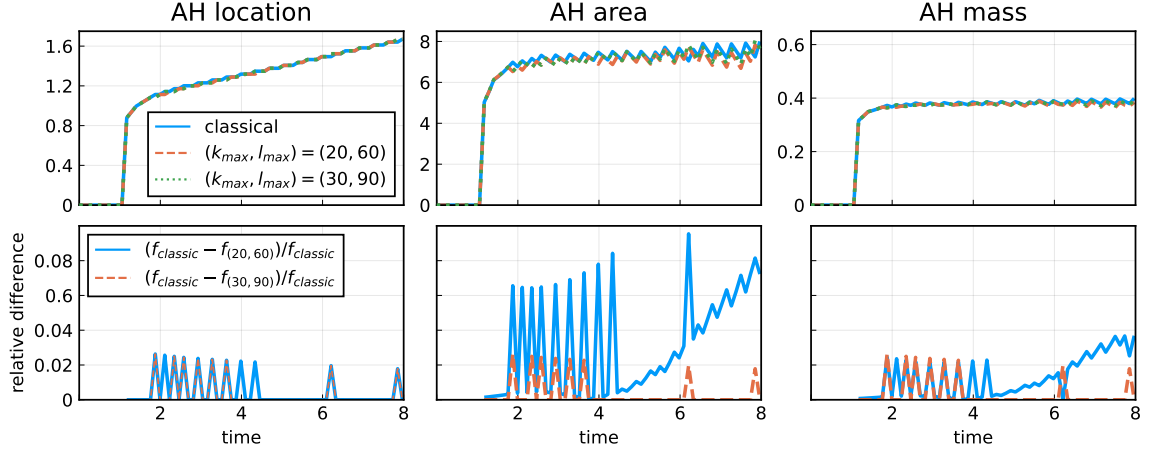


Figure 17. We compare a classical supercritical setup, against its semiclassical version with backreaction, for different values of (k_{\max}, l_{\max}) . For the initial data we consider the scalar pulse (2.18) with $a = 1.25$, $b = 0$ and $c = 1$. From left to right we present in time the location, area, and mass of the apparent horizon. The bottom row illustrates the relative difference between the semiclassical and classical setups, using the classical one as the benchmark. For all quantities we see that the relative difference between classical and semiclassical is below 10%, and decreases with increasing values of (k_{\max}, l_{\max}) .

difference in angle. It might be useful to repeat our calculation with a different gauge choice (e.g. harmonic), and examine if a different qualitative picture arises. It is also possible that calculating the two-point function at equal proper time and using proper radius instead of r could provide a picture closer to that of the analogue systems. We leave this for future work.

We should emphasize that with this setup we were not able to respect the condition $M_{\text{PV}} \gg 2\pi/\tilde{\lambda}$, given in section 4, due to numerical instability. Here we have $2\pi/\tilde{\lambda} \simeq 3.6$, which we chose for practical reasons. To respect $M_{\text{PV}} \gg 2\pi/\tilde{\lambda}$, a choice of $M_{\text{PV}} = 100$ could be more appropriate, but as explained in section 6.2 and seen in figure 14, we would not trust this simulation with backreaction and for the number of modes we can practically include. Therefore, we also do not consider it in the setup without backreaction, since it might provide misleading results. Another reason is that Hawking radiation is expected to be more intense for smaller black holes, which is what we try to form dynamically. In principle, we could perform simulations with a wider initial scalar profile, such that we respect the conditions outlined in section 4. However, such a setup either leads to a bigger black hole, or becomes unstable if the amplitude is tuned very low, in an attempt to form a smaller black hole. Maybe there is a region of the parameter space – in terms of initial data – that better respects these conditions, that more thorough exploration could reveal.

7.2 With backreaction

We repeat the supercritical simulations from the previous subsections, including backreaction. To preserve the asymptotics of the spacetime near r_{\max} we use the filter function (4.10) with $r_{\text{cut}} = 20$. We explore two backreacting setups with $(k_{\max}, l_{\max}) = \{(20, 60), (30, 90)\}$ and analyze the effect they have on the location of the apparent horizon, as well as the area and the mass of the black hole. As mentioned in subsection 2.2, we track the location of the apparent horizon r_{AH} by finding the outermost radius at which the expansion of null rays θ_{exp} vanishes. The area of the apparent horizon is defined as

$$A_{\text{AH}} := 4\pi B r_{\text{AH}}^2, \quad (7.2)$$

and the apparent horizon mass [5] as

$$M_{\text{AH}} := \frac{r_{\text{AH}}}{2} \sqrt{B|_{r_{\text{AH}}}}. \quad (7.3)$$

In figure 17 we see that all these three quantities are very similar in the classical and backreaction cases. More specifically, their relative difference is always below 10% and decrease with increasing values of k_{\max} and l_{\max} . In addition, we compare the correlation (7.1) of the case with $(k_{\max}, l_{\max}) = (30, 90)$ with backreaction, against the supercritical case without backreaction and with the same quantum modes, from the previous subsection. Qualitatively the behavior appears to be very similar. In figure 18 we demonstrate this by presenting the equal-time correlation function for $r_1 = 2.109375$, with and without backreaction. In the backreacting case we see that the oscillatory behavior around r_{AH} is more intense and that the negative value of the correlator inside the apparent horizon increases in absolute magnitude.

8 Outlook

In this paper we have introduced `SpheriCo.jl` to simulate the spherically symmetric collapse of a scalar field into a black hole, in classical and semiclassical gravity. `SpheriCo.jl` is modular, open-access and written in the `Julia` programming language. A challenge present in many studies of gravitational collapse is the approximation of the evolved variables near $r = 0$, since terms of the form $1/r$ appear in their equations of motion. This challenge becomes increasingly difficult in the semiclassical setup, where these terms can become very large and render the equations stiff. This seems to have been the main reason for driving earlier semiclassical simulations on the topic only stable for a short time. By combining the summation-by-parts operators of [21] with the convenient evolved variables of [29] we manage to perform semiclassical simulations for longer than it was previously possible, and explore quantum correlations of events across an apparent horizon.

Constraint violations can have a big impact on numerical simulations by driving the numerical solution significantly far from the physical one, or even making the simulation unstable. We attempt to control the numerical violation of the classical Hamiltonian and momentum constraints by combining the Z_4 constraint damping scheme of [32] with the system of [29]. In the latter, formally singular terms for $r = 0$ of the form $1/r$ appear,

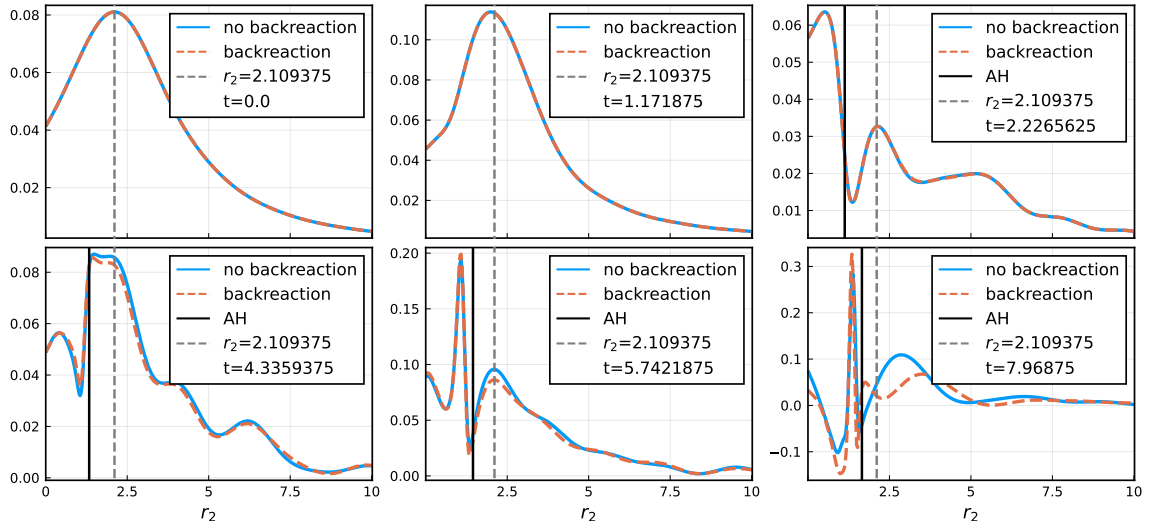


Figure 18. The real part of the correlation function (7.1) at $r_1 = 2.109375$ for a semiclassical supercritical setup with $M_{\text{PV}} = 1$ and $(k_{\text{max}}, l_{\text{max}}) = (30, 90)$, with and without backreaction. The initial scalar profile is given by (2.18) with $a = 1.25$, $b = 0$, $c = 1$. The behavior is very similar in both cases, with the backreacting one presenting slightly enhanced oscillations at late times around the location of the apparent horizon.

but are practically regular due to the specific reduction variables used. We approximate these terms with the second-order accurate summation-by-parts operators of [21]. We perform multiple tests on the classical module of our code. We recover the expected second-order convergence for both smooth and noisy data, either sub- or supercritical. We also test the performance of our implemented constraint damping scheme, which seems to be unsuccessful. More specifically, the violation of the Hamiltonian and momentum constraints with the damping scheme is equal or greater than without, or even leads to unstable simulations for certain subcritical data. We should highlight that we do not include damping of reduction constraints in our system and that we use different evolved variables than [32], features that might be responsible for this failure. One possible future improvement would be to explore the constraint damping scheme further and possibly add the damping of reduction constraints.

In terms of physical tests for the classical module, we also recover the expected near critical oscillating behavior of a scalar field, as well as the universality of the solution. This is a non-trivial result, especially given that to our knowledge the specific summation-by-parts operators have not been used again in this case, and are originally constructed for a different setup. We should also highlight that to obtain this result we had to allow our code to run with an infalling outer boundary. This is achieved numerically, since our formulation has a vanishing shift. We expect that it is numerically more economic to have a dynamic shift and perform the infalling outer boundary technique analytically. Adding the option of a dynamical shift condition could be another possible future improvement.

It could make the code more appropriate for near critical simulations, especially in the semiclassical setup, where the numerical infalling outer boundary technique seems to be unstable.

In the semiclassical setup the geometry is still classical, but the scalar field is promoted to a quantum field. To model this we utilize an expansion in spherical harmonics and radial mode functions labeled by the quantum numbers k and l , for which we solve the resulting equations of motion. The numerical approximation of the quantum field is improved with increasing number of modes included in the system. In `SpheriCo.jl` the semiclassical setup can be simulated with or without backreaction to the classical geometry. Including backreaction means the expectation value of the quantum stress-energy tensor replaces that of the classical one. To obtain a non-divergent expectation value, we use the Pauli-Villars regularization scheme, where massive ghost fields are included in the system. In theory, one would like to take the number of quantum modes, and the Pauli-Villars mass, to infinity. In practice we are limited by computational resources and the performance of our code, and truncate them to certain values. For the setup without backreaction we test our code against an exact solution for the quantum modes and recover good second-order convergence, even for high values of l , higher than those tested in [21]. To test the backreaction implementation, we examine whether we recover the Minkowski solution with smaller error, as we include more modes in the simulation. The code passes this test, but its performance depends on the value of the Pauli-Villars mass, with better performance for smaller values.

Finally, we explore the correlation of Hawking pairs around black holes, by calculating quantum two-point correlation function of the scalar in geometries with a dynamically forming apparent horizon. Our results suggest a non-trivial correlation of events inside and outside the apparent horizon. Regarding the number of quantum modes simulated, the value of the Pauli-Villars mass, and the size of the apparent horizon, we limit our simulations to setups where we trust the performance of our code, based on tests we conducted earlier. A more extended study that scans a wider region of the parameter space would be necessary to understand the phenomenon deeper, but we leave this for future work. We also highlight certain similarities and differences of our findings to those of analogue black hole systems.

Acknowledgments

We would like to thank Miguel Bezares, Carsten Gundlach, David Hilditch, Krinio Marouda and Isabel Suárez Fernández for helpful discussions, Carsten Gundlach for sharing with us his code related to the summation-by-parts operators and David Hilditch for sharing with us his notebook on the Z_4 constraint damping formulation. This work received partial support from the Science and Technology Facilities Council (STFC) [Grant Nos. ST/T000732/1, ST/X000672/1 and ST/V005596/1].

Data Access Statement

Code may be found in [27]. Data may be found in [60]. All the data were generated using SpheriCo.jl on a laptop with a 13th Gen Intel Core i7-1370P 14-core processor and 64 GB RAM. The longest simulation took around 15 clock-time hours to complete.

References

- [1] D. Christodoulou, *The Problem of a Selfgravitating Scalar Field*, *Commun. Math. Phys.* **105** (1986) 337.
- [2] D. Christodoulou, *Global Existence of Generalized Solutions of the Spherically Symmetric Einstein Scalar Equations in the Large*, *Commun. Math. Phys.* **106** (1986) 587.
- [3] D. Christodoulou, *A Mathematical Theory of Gravitational Collapse*, *Commun. Math. Phys.* **109** (1987) 613.
- [4] D. Christodoulou, *The Structure and Uniqueness of Generalized Solutions of the Spherically Symmetric Einstein Scalar Equations*, *Commun. Math. Phys.* **109** (1987) 591.
- [5] M. Alcubierre, *Introduction to 3+1 Numerical Relativity*, International Series of Monographs on Physics, OUP Oxford (2008).
- [6] M.W. Choptuik, *Universality and scaling in gravitational collapse of a massless scalar field*, *Phys. Rev. Lett.* **70** (1993) 9.
- [7] D. Garfinkle, *Choptuik scaling in null coordinates*, *Phys. Rev. D* **51** (1995) 5558 [gr-qc/9412008].
- [8] R.S. Hamade and J.M. Stewart, *The Spherically symmetric collapse of a massless scalar field*, *Class. Quant. Grav.* **13** (1996) 497 [gr-qc/9506044].
- [9] J.G. Russo, L. Susskind and L. Thorlacius, *The Endpoint of Hawking radiation*, *Phys. Rev. D* **46** (1992) 3444 [hep-th/9206070].
- [10] A. Strominger and L. Thorlacius, *Universality and scaling at the onset of quantum black hole formation*, *Phys. Rev. Lett.* **72** (1994) 1584 [hep-th/9312017].
- [11] T. Piran and A. Strominger, *Numerical analysis of black hole evaporation*, *Phys. Rev. D* **48** (1993) 4729 [hep-th/9304148].
- [12] D.A. Lowe, *Semiclassical approach to black hole evaporation*, *Phys. Rev. D* **47** (1993) 2446 [hep-th/9209008].
- [13] A. Levi and A. Ori, *Pragmatic mode-sum regularization method for semiclassical black-hole spacetimes*, *Phys. Rev. D* **91** (2015) 104028 [1503.02810].
- [14] A. Levi and A. Ori, *Mode-sum regularization of $\langle \phi^2 \rangle$ in the angular-splitting method*, *Phys. Rev. D* **94** (2016) 044054 [1606.08451].
- [15] A. Levi and A. Ori, *Versatile method for renormalized stress-energy computation in black-hole spacetimes*, *Phys. Rev. Lett.* **117** (2016) 231101 [1608.03806].
- [16] A. Levi, E. Eilon, A. Ori and M. van de Meent, *Renormalized stress-energy tensor of an evaporating spinning black hole*, *Phys. Rev. Lett.* **118** (2017) 141102 [1610.04848].
- [17] B. Berczi, P.M. Saffin and S.-Y. Zhou, *Gravitational collapse with quantum fields*, *Phys. Rev. D* **104** (2021) L041703 [2010.10142].

- [18] B. Berczi, P.M. Saffin and S.-Y. Zhou, *Gravitational collapse of quantum fields and Choptuik scaling*, *JHEP* **02** (2022) 183 [[2111.11400](#)].
- [19] J.N. Guenther, C. Hoelbling and L. Varnhorst, *Semiclassical gravitational collapse of a radially symmetric massless scalar quantum field*, *Phys. Rev. D* **105** (2022) 105010 [[2010.13215](#)].
- [20] C. Hoelbling, J.N. Guenther and L. Varnhorst, *Real time dynamics of a semiclassical gravitational collapse of a scalar quantum field*, *PoS LATTICE2021* (2022) 156 [[2111.15562](#)].
- [21] C. Gundlach, J.M. Martin-Garcia and D. Garfinkle, *Summation by parts methods for spherical harmonic decompositions of the wave equation in any dimensions*, *Class. Quant. Grav.* **30** (2013) 145003 [[1010.2427](#)].
- [22] S.W. Hawking, *Particle Creation by Black Holes*, *Commun. Math. Phys.* **43** (1975) 199.
- [23] R. Schutzhold and W.G. Unruh, *On Quantum Correlations across the Black Hole Horizon*, *Phys. Rev. D* **81** (2010) 124033 [[1002.1844](#)].
- [24] M. Fontana and M. Rinaldi, *Stress-energy tensor correlations across regular black holes horizons*, *Phys. Rev. D* **108** (2023) 125003 [[2302.08804](#)].
- [25] I. Carusotto, S. Fagnocchi, A. Recati, R. Balbinot and A. Fabbri, *Numerical observation of Hawking radiation from acoustic black holes in atomic BECs*, *New J. Phys.* **10** (2008) 103001 [[0803.0507](#)].
- [26] R. Balbinot and A. Fabbri, *Quantum correlations across the horizon in acoustic and gravitational black holes*, *Phys. Rev. D* **105** (2022) 045010 [[2107.00702](#)].
- [27] “Spherico.jl.” <https://github.com/ThanasisGiannakopoulos/SpheriCo.jl>.
- [28] J. Bezanson, A. Edelman, S. Karpinski and V.B. Shah, *Julia: A fresh approach to numerical computing*, *SIAM Review* **59** (2017) 65 [<https://doi.org/10.1137/141000671>].
- [29] M. Alcubierre and J.A. Gonzalez, *Regularization of spherically symmetric evolution codes in numerical relativity*, *Comput. Phys. Commun.* **167** (2005) 76 [[gr-qc/0401113](#)].
- [30] F. Pretorius, *Evolution of binary black hole spacetimes*, *Phys. Rev. Lett.* **95** (2005) 121101 [[gr-qc/0507014](#)].
- [31] C. Gundlach, J.M. Martin-Garcia, G. Calabrese and I. Hinder, *Constraint damping in the Z_4 formulation and harmonic gauge*, *Class. Quant. Grav.* **22** (2005) 3767 [[gr-qc/0504114](#)].
- [32] S. Bernuzzi and D. Hilditch, *Constraint violation in free evolution schemes: Comparing BSSNOK with a conformal decomposition of Z_4* , *Phys. Rev. D* **81** (2010) 084003 [[0912.2920](#)].
- [33] C. Bona, T. Ledvinka, C. Palenzuela and M. Zacek, *General covariant evolution formalism for numerical relativity*, *Phys. Rev. D* **67** (2003) 104005 [[gr-qc/0302083](#)].
- [34] C. Bona and C. Palenzuela, *Dynamical shift conditions for the Z_4 and BSSN hyperbolic formalisms*, *Phys. Rev. D* **69** (2004) 104003 [[gr-qc/0401019](#)].
- [35] C. Bona, J. Masso, E. Seidel and J. Stela, *A New formalism for numerical relativity*, *Phys. Rev. Lett.* **75** (1995) 600 [[gr-qc/9412071](#)].
- [36] P. Anninos, K. Camarda, J. Masso, E. Seidel, W.-M. Suen and J. Towns, *Three-dimensional numerical relativity: The Evolution of black holes*, *Phys. Rev. D* **52** (1995) 2059 [[gr-qc/9503025](#)].

- [37] V. Cardoso, D. Hilditch, K. Marouda, J. Natário and U. Sperhake, *Curvature and dynamical spacetimes: can we peer into the quantum regime?*, *Class. Quant. Grav.* **40** (2023) 065008 [[2209.12589](#)].
- [38] L. Pareschi and G. Russo, *Implicit-explicit runge-kutta schemes for stiff systems of differential equations*, in *Recent Trends in Numerical Analysis*, (USA), p. 269–288, Nova Science Publishers, Inc. (2000).
- [39] C.R. Evans, *An Approach for Calculating Axisymmetric Gravitational Collapse*, phd thesis, University of Texas at Austin, 1984. Available at https://users.physics.unc.edu/~evans/cr_evans_thesis_1984.pdf.
- [40] I. Suárez Fernández, R. Vicente and D. Hilditch, *Semilinear wave model for critical collapse*, *Phys. Rev. D* **103** (2021) 044016 [[2007.13764](#)].
- [41] B. Gustafsson, H.-O. Kreiss and J. Olinger, *Time dependent problems and difference methods*, Wiley, New York (1995).
- [42] H. Kreiss and J. Olinger, *Methods for the approximate solution of time dependent problems*, GARP Publications Series, SELBSTVERL.) FEBR (1973).
- [43] “Interpolations.jl.” <https://github.com/JuliaMath/Interpolations.jl>.
- [44] O. Rinne, *Type II critical collapse on a single fixed grid: a gauge-driven ingoing boundary method*, *Gen. Rel. Grav.* **52** (2020) 117 [[2008.12726](#)].
- [45] D. Cors, S. Renkhoff, H.R. Rüter, D. Hilditch and B. Brügmann, *Formulation improvements for critical collapse simulations*, *Phys. Rev. D* **108** (2023) 124021 [[2308.01812](#)].
- [46] M. Alcubierre et al., *Toward standard testbeds for numerical relativity*, *Class. Quant. Grav.* **21** (2004) 589 [[gr-qc/0305023](#)].
- [47] G. Calabrese, I. Hinder and S. Husa, *Numerical stability for finite difference approximations of Einstein’s equations*, *J. Comput. Phys.* **218** (2006) 607 [[gr-qc/0503056](#)].
- [48] H. Witek, D. Hilditch and U. Sperhake, *Stability of the puncture method with a generalized baumgarte-shapiro-shibata-nakamura formulation*, *Phys. Rev. D* **83** (2011) 104041.
- [49] Z. Cao and D. Hilditch, *Numerical stability of the Z4c formulation of general relativity*, *Phys. Rev. D* **85** (2012) 124032 [[1111.2177](#)].
- [50] M.C. Babiuc et al., *Implementation of standard testbeds for numerical relativity*, *Class. Quant. Grav.* **25** (2008) 125012 [[0709.3559](#)].
- [51] T. Giannakopoulos, *Characteristic formulations of general relativity and applications*, Ph.D. thesis, Instituto Superior Técnico, Lisbon, 8, 2023. [2308.16001](#).
- [52] I. Hinder, *Well-posed formulations and stable finite differencing schemes for numerical relativity*, Ph.D. thesis, U. Southampton (main), 2005. 10.5258/SOTON/393564.
- [53] C. Gundlach and J.M. Martin-Garcia, *Critical phenomena in gravitational collapse*, *Living Rev. Rel.* **10** (2007) 5 [[0711.4620](#)].
- [54] T.W. Baumgarte, *Aspherical deformations of the Choptuik spacetime*, *Phys. Rev. D* **98** (2018) 084012 [[1807.10342](#)].
- [55] K. Marouda, D. Cors, H.R. Rüter, F. Atteneder and D. Hilditch, *Twist-free axisymmetric critical collapse of a complex scalar field*, *Phys. Rev. D* **109** (2024) 124042 [[2402.06724](#)].
- [56] E. Jimenez-Vazquez and M. Alcubierre, *Critical gravitational collapse of a massive complex*

scalar field, *Phys. Rev. D* **106** (2022) 044071 [2206.01389].

- [57] “Simulations from SpheriCo.jl.” https://youtube.com/playlist?list=PLYJ_PP8q0GF8pj5YvAKoQH0c9wp6fSUNk&si=ZDa-8cMwWSRHhBV.
- [58] J. Steinhauer, *Observation of quantum Hawking radiation and its entanglement in an analogue black hole*, *Nature Phys.* **12** (2016) 959 [1510.00621].
- [59] M.J. Jacquet, M. Joly, L. Giacomelli, F. Claude, Q. Glorieux, A. Bramati et al., *Analogue quantum simulation of the Hawking effect in a polariton superfluid*, *Eur. Phys. J. D* **76** (2022) 152 [2201.02038].
- [60] B. Berdzi, M. Eriksson, T. Giannakopoulos and P. Saffin, *Quantum correlations in a gravitational collapse simulation with SpheriCo.jl: data*, 12, 2024. <https://doi.org/10.5281/zenodo.14365566>.
- [61] S. Pla and E. Winstanley, *Equivalence of the adiabatic expansion and Hadamard renormalization for a charged scalar field*, *Phys. Rev. D* **107** (2023) 025004 [2209.01079].
- [62] J. Baacke, K. Heitmann and C. Patzold, *Renormalization of nonequilibrium dynamics in FRW cosmology*, *Phys. Rev. D* **56** (1997) 6556 [hep-ph/9706274].
- [63] J. Baacke and C. Patzold, *Out-of-equilibrium evolution of scalar fields in FRW cosmology: Renormalization and numerical simulations*, *Phys. Rev. D* **61** (2000) 024016 [hep-ph/9906417].
- [64] T. Markkanen and A. Tranberg, *A Simple Method for One-Loop Renormalization in Curved Space-Time*, *JCAP* **08** (2013) 045 [1303.0180].
- [65] J.P. Paz and F.D. Mazzitelli, *Renormalized Evolution Equations for the Back Reaction Problem With a Selfinteracting Scalar Field*, *Phys. Rev. D* **37** (1988) 2170.

A Hyperbolicity of the classical system

The hyperbolicity of a partial differential equation (PDE) system is connected to the well-posedness of the corresponding PDE problem, which is a necessary condition for trustable numerical simulations. It can also be used to understand what are appropriate boundary conditions for a specific problem. To study the hyperbolicity of the evolved system (2.13)–(2.14), we linearise it around an arbitrary background

$$\mathbf{u}_0 = \left(\Phi_0, \Pi_0, \Psi_0, A_0, B_0, D_{B0}, \tilde{U}_0, K_0, K_{B0}, \lambda_0, \alpha_0, D_{\alpha 0}, \Theta_0, Z_{r0} \right)^T, \quad (\text{A.1})$$

and work in the constant coefficient approximation [42]. Since the Einstein equations are quasi-linear (i.e. linear in highest derivatives), the degree of hyperbolicity of the system is the same as its corresponding linear system (A.1). The linearised Einstein equations can then be written as

$$\dot{\mathbf{u}} = \mathbf{A}^r(\mathbf{u}_0) \mathbf{u}' + \mathbf{S}(r, \mathbf{u}, \mathbf{u}_0, \mathbf{u}'_0), \quad (\text{A.2})$$

where \mathbf{A}^r is the principal part matrix containing the coefficients of the first-order (radial) derivative of \mathbf{u} , and \mathbf{S} only containing lower-order (in derivatives) terms. The linearised system can be brought into the form

$$\dot{\mathbf{v}} \simeq \mathbf{J}^r(\mathbf{u}_0) \mathbf{v}', \quad (\text{A.3})$$

where \simeq denotes equality in the principal terms and

$$\begin{aligned} \mathbf{J}^r(\mathbf{u}_0) &:= \mathbf{T}^{-1}(\mathbf{u}_0) \mathbf{A}^r(\mathbf{u}_0) \mathbf{T}(\mathbf{u}_0) \\ &= \text{diag} \left(0, 0, 0, 0, 0, 0, -\sqrt{\frac{2\alpha_0}{A_0}}, \sqrt{\frac{2\alpha_0}{A_0}}, -\frac{\alpha_0}{\sqrt{A_0}}, -\frac{\alpha_0}{\sqrt{A_0}}, -\frac{\alpha_0}{\sqrt{A_0}}, \frac{\alpha_0}{\sqrt{A_0}}, \frac{\alpha_0}{\sqrt{A_0}}, \frac{\alpha_0}{\sqrt{A_0}} \right), \end{aligned} \quad (\text{A.4})$$

is the Jordan normal form of \mathbf{A}^r , \mathbf{T} is the transformation matrix and $\mathbf{v} := \mathbf{T}^{-1}(\mathbf{u}_0) \mathbf{u}$ is a vector containing the characteristic variables of the system. If \mathbf{J}^r is real and diagonal, then the system (A.2) is called strongly hyperbolic and each characteristic variable satisfies an advection equation up to lower order terms.

The eigenvalues \mathcal{E}_i of \mathbf{A}^r (entries of \mathbf{J}^r) determine the radial propagation speeds of the characteristic variables (entries of \mathbf{v}) and are referred to as the characteristic speeds of the system. In a spherically symmetric spacetime, stationary modes ($\mathcal{E}_i = 0$) do not propagate radially. Outgoing modes ($\mathcal{E}_i < 0$) propagate outward towards increasing r and ingoing modes ($\mathcal{E}_i > 0$) propagate inward towards decreasing r . The static, outgoing and ingoing modes corresponding to (A.4) are

$$\mathbf{v}_{\text{stat}} = \left(-\alpha_0 D_\alpha - 4D_B + \tilde{U} + 4Z_r, \frac{A_0 D_B}{B_0} + \lambda, \alpha, B, A, \Phi \right)^T, \quad (\text{A.5})$$

and

$$\mathbf{v}_{\text{out}} = (v_{\text{out},1}, v_{\text{out},2}, v_{\text{out},3}, v_{\text{out},4})^T, \quad \mathbf{v}_{\text{in}} = (v_{\text{in},1}, v_{\text{in},2}, v_{\text{in},3}, v_{\text{in},4})^T, \quad (\text{A.6})$$

with

$$\begin{aligned} v_{\text{out},1} &= \frac{1}{2\alpha_0 - 4} \left\{ \sqrt{2A_0\alpha_0} [K(\alpha_0 - 2) - 4K_B\alpha_0 + 2(\alpha_0 + 2)\Theta] \right. \\ &\quad \left. + \alpha_0 [D_\alpha(\alpha_0 - 2) + 4D_B - 8Z_r] \right\}, \\ v_{\text{out},2} &= \frac{1}{2} \left[\sqrt{A_0} (2K_B - \Theta) + Z_r \right], \\ v_{\text{out},3} &= \frac{\sqrt{A_0}\Theta + D_B - Z_r}{2\sqrt{A_0}}, \\ v_{\text{out},4} &= \frac{1}{2} (\Pi - B_0\Psi), \end{aligned} \quad (\text{A.7})$$

and

$$\begin{aligned} v_{\text{in},1} &= \frac{1}{2\alpha_0 - 4} \left\{ -\sqrt{2A_0\alpha_0} [K(\alpha_0 - 2) - 4K_B\alpha_0 + 2(\alpha_0 + 2)\Theta] \right. \\ &\quad \left. + \alpha_0 [D_\alpha(\alpha_0 - 2) + 4D_B - 8Z_r] \right\}, \\ v_{\text{in},2} &= \frac{1}{2} \left[\sqrt{A_0} (\Theta - 2K_B) + Z_r \right], \\ v_{\text{in},3} &= \frac{\sqrt{A_0}\Theta - D_B + Z_r}{2\sqrt{A_0}}, \\ v_{\text{in},4} &= \frac{1}{2} (\Pi + B_0\Psi). \end{aligned} \quad (\text{A.8})$$

In order to obtain boundary conditions using the above analysis, the background values (A.1) are replaced with the evolved variables. We expect these values to be close to the

Minkowski solution for the spatial region near r_{\max} , provided that r_{\max} is placed far enough from the centre of the scalar Gaussian profile.

When the classical evolution system (2.13)–(2.14) is strongly hyperbolic, its initial value problem is well-posed in the L^2 -norm [41], i.e.,

$$\|\mathbf{u}(t, r)\| \leq c_1 e^{c_2 t} \|\mathbf{u}(0, r)\|, \quad (\text{A.9})$$

for some constants $c_1 \geq 1$ and $c_2 \in \mathbb{R}$, with

$$\|\mathbf{u}(t, r)\|^2 = \int_0^r dr' \sum_i u_i^2(t, r'), \quad (\text{A.10})$$

where i denotes the elements of \mathbf{u} . In subsections 5.1 and 5.2 we utilise the norm (A.10) to perform convergence tests, where we take $r = r_{\text{causal}}$, which is the maximum value of r that is causally disconnected from r_{\max} .

B Double null co-ordinates for postprocessing

While the line element (2.1) is useful for the simulation, double-null co-ordinates are useful for understanding the global structure of the geometry. This also gives another natural set of co-ordinates in which to look at $\langle \hat{\Phi} \hat{\Phi} \rangle$ correlators, namely correlators along a null surface. For this reason, we added in `SpheriCo.jl` the option for the following post-processing calculation. We start by writing the line element as

$$ds^2 = - \left[\alpha(t, r) dt - \sqrt{A(t, r)} dr \right] \left[\alpha(t, r) dt + \sqrt{A(t, r)} dr \right] + r^2 B(t, r) d\Omega, \quad (\text{B.1})$$

and introduce new co-ordinates $U(t, r)$, $V(t, r)$ defined by

$$\frac{1}{f(t, r)} dU = \alpha(t, r) dt - \sqrt{A(t, r)} dr, \quad (\text{B.2})$$

$$\frac{1}{g(t, r)} dV = \alpha(t, r) dt + \sqrt{A(t, r)} dr, \quad (\text{B.3})$$

for some f and g to be determined. This leads to

$$ds^2 = - \frac{dU dV}{fg} + r^2 B(t, r) d\Omega. \quad (\text{B.4})$$

Now we take the defining relations (B.2), (B.3) to find

$$\alpha f = \frac{\partial U}{\partial t}, \quad -f \sqrt{A} = \frac{\partial U}{\partial r}, \quad (\text{B.5})$$

$$\alpha g = \frac{\partial V}{\partial t}, \quad g \sqrt{A} = \frac{\partial V}{\partial r}, \quad (\text{B.6})$$

noting that integrability requires

$$\frac{\partial}{\partial r} \frac{\partial U}{\partial t} = \frac{\partial}{\partial t} \frac{\partial U}{\partial r}, \quad \frac{\partial}{\partial r} \frac{\partial V}{\partial t} = \frac{\partial}{\partial t} \frac{\partial V}{\partial r}, \quad (\text{B.7})$$

which leads to

$$\frac{\partial}{\partial t} f = -\frac{\partial_r(\alpha f) + f\partial_t\sqrt{A}}{\sqrt{A}}, \quad (\text{B.8})$$

$$\frac{\partial}{\partial t} g = -\frac{\partial_r(\alpha g) - g\partial_t\sqrt{A}}{\sqrt{A}}. \quad (\text{B.9})$$

These differential equations for $f(t, r)$ and $g(t, r)$ may be solved once initial profiles for them have been set. A natural choice is $f(t=0, r) = g(t=0, r) = 1$ and we furthermore choose $U(t=0, r=0) = V(t=0, r=0) = 0$. Now we have initial data for $U(t, r)$ and $V(t, r)$, we may evolve to find $U(t, r)$, $V(t, r)$ using the time evolution equations in (B.5) and (B.6). For convenience, we solve the evolution equations (B.5), (B.6), (B.8) and (B.9) together with our classical system (2.14), and store the respective variables.

C Pauli-Villars counterterms

The UV divergences contained in the expectation values of the stress-energy tensor can be cancelled using metric and curvature tensors, as expressed in (3.8). The coefficients of these counterterms are therefore independent of the background metric they are computed in. However, since some metrics have vanishing curvature tensors, not all metrics are appropriate to determine all possible counterterms. For instance, in Minkowski spacetime, only the cosmological constant Λ in (3.8) can be computed. Interesting discussions on regularization in curved spacetimes may be found in [61–64].

A relatively simple metric choice with non-vanishing curvature tensors is the FRW metric,

$$ds^2 = -dt^2 + a^2(t)d\mathbf{x}^2, \quad (\text{C.1})$$

where $a(t)$ is the scale factor. In this case, the regularized stress-tensor can be written

$$T_{ab}^{\text{reg}} = \langle \chi | \hat{T}_{ab} | \chi \rangle + \Lambda g_{ab} + \delta M_{\text{Pl}}^2 G_{ab} + \delta\epsilon_1 H_{ab}^{(1)} + \delta\epsilon_2 H_{ab}^{(2)} + \delta\epsilon_3 H_{ab}, \quad (\text{C.2})$$

where the $\mathcal{O}(R^2)$ gravitational terms $H_{ab}^{(1)}$, $H_{ab}^{(2)}$ and H_{ab} can be found in [65]. On dimensional grounds we expect that the counterterms depend on the Pauli-Villars mass as $\Lambda \propto M_{\text{PV}}^4$, $\delta M_{\text{Pl}}^2 \propto M_{\text{PV}}^2$ and $\delta\epsilon_{1,2,3} \propto \ln M_{\text{PV}}$. As in section 3.2, we set the renormalisation condition that $\delta\epsilon_{1,2,3} = 0$ for the range of Pauli-Villars masses considered.

To compute the counterterms Λ and δM_{Pl}^2 we consider a free massive scalar field $\hat{\phi}$, with mode expansion

$$\hat{\phi}(t, \mathbf{x}) = \int d^3\mathbf{k} \left[\hat{a}_k u_k(t) e^{i\mathbf{k}\cdot\mathbf{x}} + \hat{a}_k^\dagger u_k^*(t) e^{-i\mathbf{k}\cdot\mathbf{x}} \right], \quad (\text{C.3})$$

where the modes satisfy the equation of motion

$$\ddot{u}_k + 3H\dot{u}_k + \mu^2 u_k^2 = 0, \quad (\text{C.4})$$

where $H := \dot{a}/a$ is the Hubble constant. The conjugate momentum is $\hat{\pi} = a^3 \dot{\hat{\phi}}$ and fulfils the commutation relations $[\hat{\phi}(t, \mathbf{x}) \hat{\pi}(t', \mathbf{x}')] = \frac{i}{a^3(t)} \delta^{(3)}(\mathbf{x} - \mathbf{x}')$, where the normalisation has been chosen according to $[\hat{a}_k, \hat{a}_{k'}^\dagger] = \delta^{(3)}(\mathbf{k} - \mathbf{k}')$.

In terms of the modes u_k , the expectation values of the stress-energy tensor components are

$$\langle \chi | \hat{T}_{00} | \chi \rangle = \int d^3k \frac{1}{2} \left[|\dot{u}_k|^2 + \frac{k^2}{a^2} |u_k|^2 + \mu^2 |u_k|^2 \right], \quad (\text{C.5a})$$

$$\langle \chi | \hat{T}^i_i | \chi \rangle = \int d^3k \frac{1}{2} \left[3|\dot{u}_k|^2 - \frac{k^2}{a^2} |u_k|^2 - 3\mu^2 |u_k|^2 \right], \quad (\text{C.5b})$$

Assuming the background to be slowly varying, we may use the WKB approximation for the mode functions,

$$u_k(t) = \frac{1}{\sqrt{2(2\pi)^3 a^3(t) W(t)}} e^{-i \int^t dt' W(t')}, \quad (\text{C.6})$$

where the equation of motion (C.4) leads to an equation for $W(t)$,

$$W^2 = \omega_k^2 - \frac{3}{2} \frac{\ddot{a}}{a} - \frac{3}{4} H^2 + \frac{3\dot{W}^2}{4W^2} - \frac{\ddot{W}}{2W}, \quad (\text{C.7})$$

with $\omega_k^2 := k^2/a^2 + \mu^2$. This can be solved iteratively, where at zeroth adiabatic order $W_{(0)}^2 = \omega_k^2$. Substituting $W_{(0)}^2$ into the right-hand side of (C.7), we find to the next order

$$\begin{aligned} W_{(0)}^2 + W_{(2)}^2 &= \omega_k^2 - \frac{3}{2} \frac{\ddot{a}}{a} - \frac{3}{4} H^2 + \frac{3\dot{\omega}_k^2}{4\omega_k^2} - \frac{\ddot{\omega}_k}{2\omega_k} \\ &= \omega_k^2 - \frac{2\omega_k^2 + \mu^2}{2\omega_k^2} \frac{\ddot{a}}{a} - \frac{4\omega_k^4 + 4\mu^2\omega_k^2 - 5\mu^4}{4\omega_k^4} H^2, \end{aligned} \quad (\text{C.8})$$

where we have expressed $\dot{\omega}_k$ and $\ddot{\omega}_k$ in terms of a and \ddot{a} using the dispersion relation. In principle one may continue to higher WKB order, but it will be necessary to only compute the counterterms Λ and δM_{Pl}^2 . We can then set (C.8) as our approximation for W^2 and use it to compute the stress-energy components in (C.5). Here we note that, at this order in the adiabatic expansion,

$$\frac{\dot{W}}{W} = -\frac{\omega_k^2 - \mu^2}{\omega_k^2} H, \quad \frac{1}{W} = \frac{1}{\omega_k} \left[1 - \frac{W_{(2)}^2}{2\omega_k^2} \right]. \quad (\text{C.9})$$

For the temporal component of the stress-energy tensor (C.5a), we have

$$\langle \chi | \hat{T}_{00} | \chi \rangle = \int \frac{dk k^2}{(2\pi)^2 a^3} \left[\sqrt{k^2/a^2 + \mu^2} + \frac{H^2 (2k^2/a^2 + 3\mu^2)^2}{8 (k^2/a^2 + \mu^2)^{5/2}} \right]. \quad (\text{C.10})$$

The above expression applies to a single scalar field. For our system with a physical massless scalar and five additional Pauli-Villars ghost fields with masses as in (3.12), the first integral in (C.10) becomes proportional to

$$\int_0^\infty d\xi \xi^2 \left(\xi - 2\sqrt{\xi^2 + 1} + 2\sqrt{\xi^2 + 3} - \sqrt{\xi^2 + 4} \right) = \frac{1}{8} \ln \left(\frac{3^9}{2^{16}} \right), \quad (\text{C.11})$$

with $\xi := k/(aM_{\text{PV}})$. Similarly, for the second integral,

$$\int d\xi \xi^2 \left(\frac{4}{\xi} - 2 \frac{(2\xi^2 + 3)^2}{(\xi^2 + 1)^{5/2}} + 2 \frac{(2\xi^2 + 9)^2}{(\xi^2 + 3)^{5/2}} - \frac{(2\xi^2 + 12)^2}{(\xi^2 + 4)^{5/2}} \right) = \ln \left(\frac{2^8}{3^6} \right). \quad (\text{C.12})$$

Collecting these terms, we find

$$\begin{aligned}\langle \chi | \hat{T}_{00} | \chi \rangle &= \frac{M_{\text{PV}}^4}{8(2\pi)^2} \ln \left(\frac{3^9}{2^{16}} \right) + \frac{M_{\text{PV}}^2}{24(2\pi)^2} \ln \left(\frac{2^8}{3^6} \right) 3H^2 \\ &= -\frac{M_{\text{PV}}^4}{8(2\pi)^2} \ln \left(\frac{3^9}{2^{16}} \right) g_{00} + \frac{M_{\text{PV}}^2}{24(2\pi)^2} \ln \left(\frac{2^8}{3^6} \right) G_{00},\end{aligned}\tag{C.13}$$

where on the second row we have expressed the result in terms of the metric and Einstein tensor component in FRW spacetime, $G_{00} = 3H^2$.

For the spatial part of the stress-energy tensor (C.5b), we have

$$\begin{aligned}\langle \chi | \hat{T}^i_i | \chi \rangle &= \int \frac{d^3\mathbf{k}}{(2\pi)^3} \frac{1}{a^3\omega_k} \left[\frac{\omega_k^2 - \mu^2}{2} + \frac{H^2}{16} \frac{(2\omega_k^2 + \mu^2)(2\omega_k^4 - m^2\omega_k^2 + 5\mu^4)}{\omega_k^6} - \frac{(2\omega_k^2 + \mu^2)^2}{8\omega_k^4} \frac{\ddot{a}}{a} \right] \\ &= \int \frac{d^3\mathbf{k}}{(2\pi)^3} \frac{1}{a^3\omega_k} \left[\frac{1}{2}\tilde{k}^2 + \frac{H^2}{16} \frac{(2\tilde{k}^2 + 3\mu^2)(2\tilde{k}^4 + 3\mu^2\tilde{k}^2 + 6\mu^4)}{(\tilde{k}^2 + \mu^2)^3} - \frac{(2\tilde{k}^2 + 3\mu^2)^2}{8(\tilde{k}^2 + \mu^2)^2} \frac{\ddot{a}}{a} \right],\end{aligned}\tag{C.14}$$

where $\tilde{k} := k/a$. Including the Pauli-Villars fields, we may compute (C.14) analogously to (C.10), to obtain

$$\begin{aligned}\langle \chi | \hat{T}^i_i | \chi \rangle &= -3\frac{M_{\text{PV}}^4}{8(2\pi)^2} \ln \left(\frac{3^9}{2^{16}} \right) - \frac{M_{\text{PV}}^2}{24(2\pi)^2} \ln \left(\frac{2^8}{3^6} \right) 3H^2 - \frac{M_{\text{PV}}^2}{24(2\pi)^2} \ln \left(\frac{2^8}{3^6} \right) \frac{6\ddot{a}}{a} \\ &= -\frac{M_{\text{PV}}^4}{8(2\pi)^2} \ln \left(\frac{3^9}{2^{16}} \right) \eta^i_i + \frac{M_{\text{PV}}^2}{24(2\pi)^2} \ln \left(\frac{2^8}{3^6} \right) G^i_i.\end{aligned}\tag{C.15}$$

where we have used $G^i_i = -3[H^2 + 2\frac{\ddot{a}}{a}]$. Hence, we recover the result (3.13) for the regularized stress-energy tensor, which sets the counterterms according to (3.14).

D Additional code testing

Convergence and robust stability. We repeat the convergence tests of subsection 5.1 for the classical setup. The given data are the same, the difference is that there is artificial dissipation with $\sigma = 0.02$. We see good second-order convergence for both super- and subcritical data, pointwisely and in the L^2 -norm of the evolved system. We also repeat the robust stability tests of subsection 5.2, with artificial dissipation $\sigma = 0.02$ and random noise amplitude $A_{h_D} = 10^{-3}/4^D$ in figure 22, as well as no artificial dissipation and $A_{h_D} = 10^{-5}/4^D$ in figure 23. In both cases the convergence rate is improved in comparison to the results of figure 4. This is expected for both instances: for the former, artificial dissipation is designed to reduce noise and for the latter, the lower amplitude of the random noise means that all resolutions apart from $D = 3$ have an amplitude A_{h_D} which is below round-off error when squared. Consequently, only the linear part of the evolution system is probed with amplitude.

Critical phenomena. We report the results of ID family 2 with $b = 5$ and $c = 1$ in the initial profile of Φ in (2.18). For these runs we choose $r_{\text{max}} = 11.76$, $t_{\text{max}} = 11.75$ and dissipation with $\sigma = 0.02$. As in subsection 5.4, the radial grid has $N_r = 128 \cdot 2^D + 3$ points,

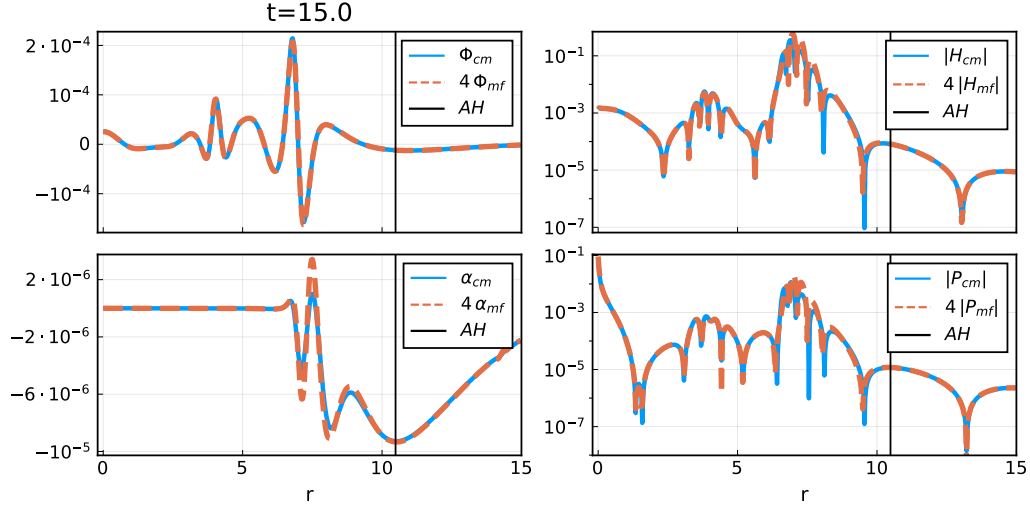


Figure 19. Supercritical data: pointwise convergence for $\Phi, \alpha, |H|, |P|$ at t_{\max} , for evolution with artificial dissipation $\sigma = 0.02$. We interpret the overlap of the rescaled grid functions as evidence for good second-order convergence, as in the case with no artificial dissipation.

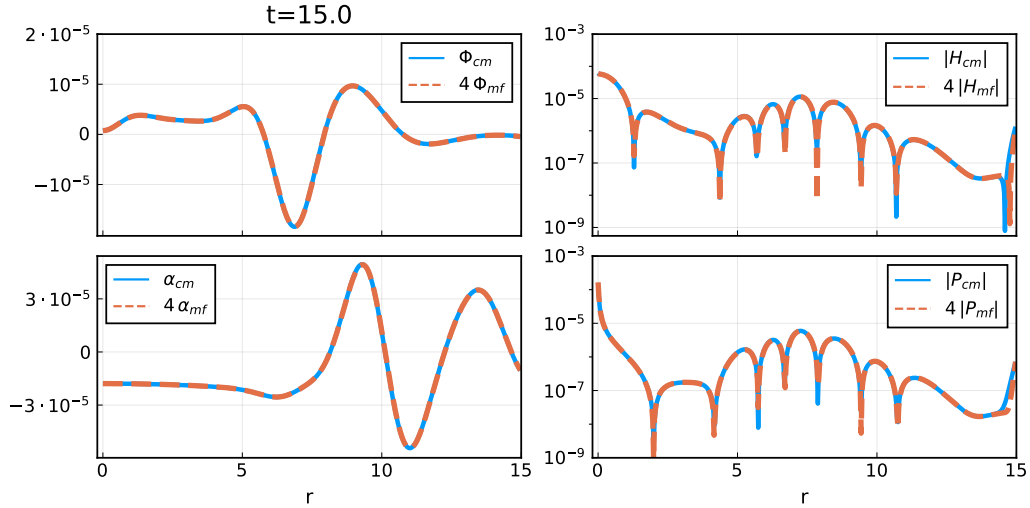


Figure 20. Subcritical data: pointwise convergence for $\Phi, \alpha, |H|, |P|$ at t_{\max} , for an evolution with artificial dissipation $\sigma = 0.02$. The code exhibits second order convergence.

with $D = \{5, 6, 7\}$. We find that the critical amplitude is $a_* \in (0.044900, 0.044901)$ and in figure 24 we show the value of the classical scalar field Φ at $r = 0$ against the similarity time T defined in (5.7), as well as the Ricci scalar R , Hamiltonian and momentum constraint violations and differences $A - B$ and $K_A - K_B$. The results are qualitatively the same as for ID family 1, with the scalar field oscillating again between ± 0.6 , as expected from the universality of the near critical spherically symmetric solutions. In figure 25 we demonstrate the second-order convergence for Φ and α at $r = 0$.

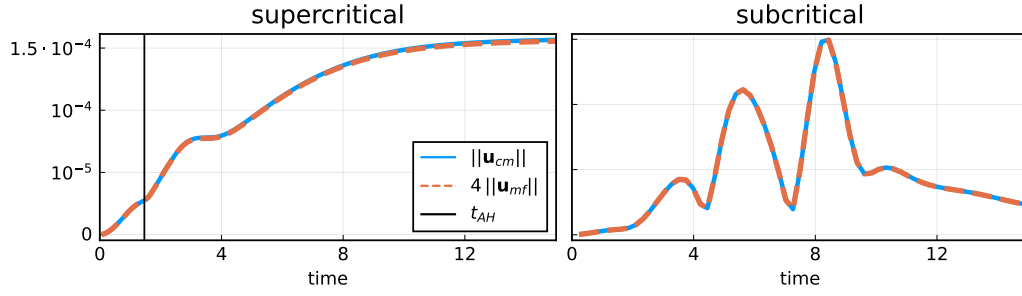


Figure 21. Norm convergence for supercritical (left) and subcritical (right) data, with smooth initial data, for an evolution with artificial dissipation $\sigma = 0.02$. Both setups exhibit good second-order convergence, indicated by the good overlap of the rescaled norms.

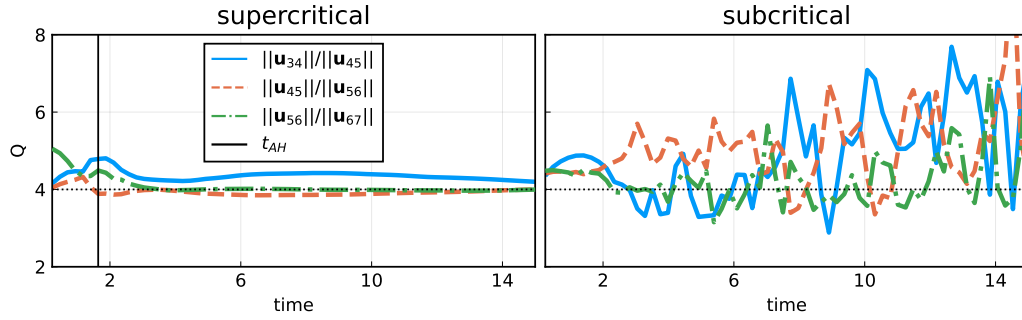


Figure 22. Robust stability tests for supercritical (left) and subcritical (right) data with $A_{h_D} = 10^{-3}/4^D$ and artificial dissipation $\sigma = 0.02$.

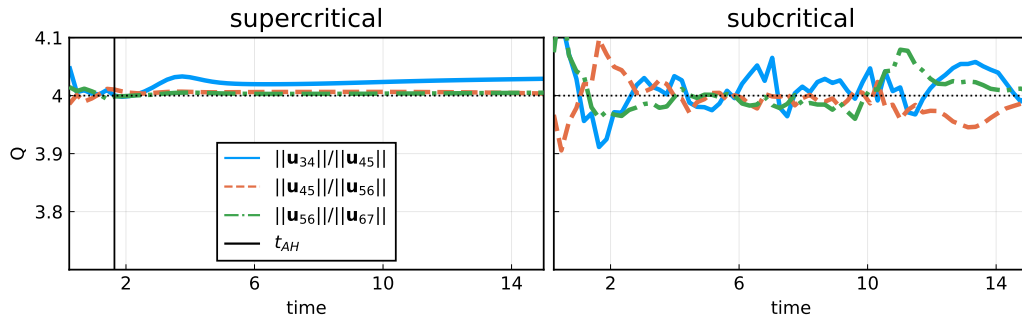


Figure 23. Robust stability tests for supercritical (left) and subcritical (right) data with $A_{h_D} = 10^{-5}/4^D$ and no artificial dissipation.

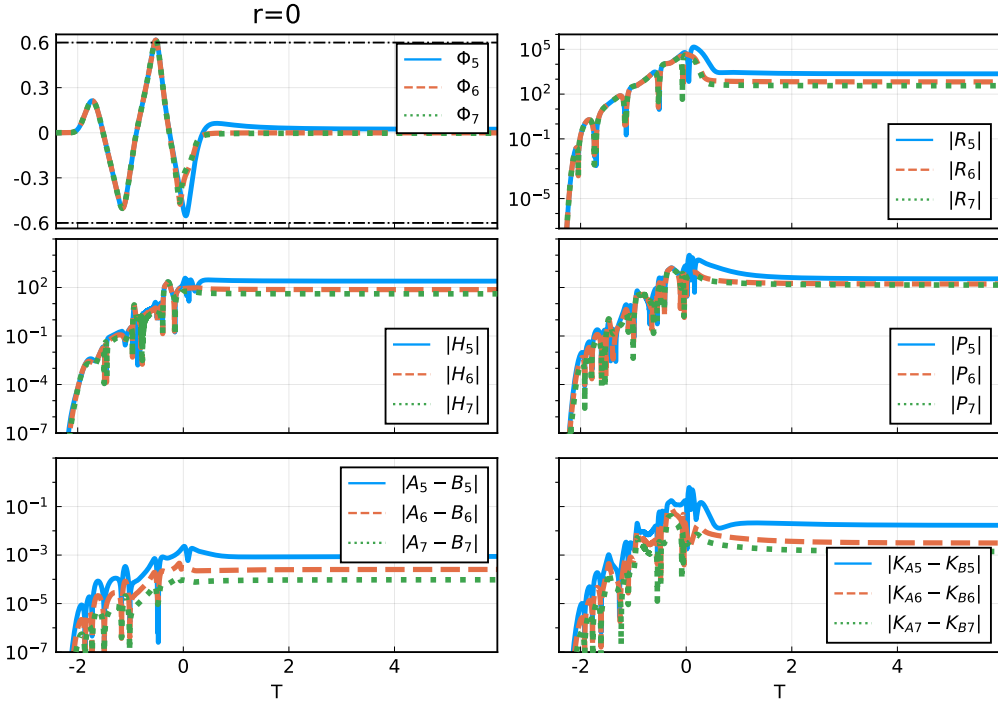


Figure 24. The different quantities monitored against the similarity time T as defined in (5.7), at $r = 0$, for three different resolutions labelled by $D = \{5, 6, 7\}$. Top left: the scalar field, top right: the absolute value of the Ricci scalar R . Middle: the absolute value of the Hamiltonian H and momentum P constraints on the left and right, respectively. Bottom: the absolute value of the difference between the metric function A, B (left) and the extrinsic curvature components K_A, K_B (right).

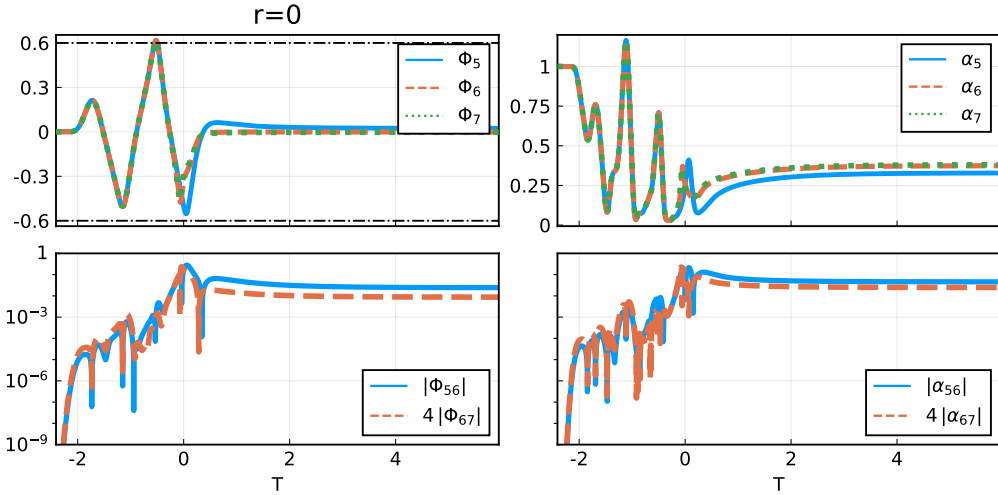


Figure 25. Pointwise convergence at $r = 0$ for the classical scalar field Φ (left) and the lapse function α (right), as a function of the similarity time T . The different resolutions $D = \{5, 6, 7\}$ are denoted with the respective D in the subscript. The numerical error (bottom) is computed by taking the difference between the numerical solutions of two different resolutions, denoted by both their D labels in the subscript.